



The Leading Intraseasonal Variability Mode of Wintertime Surface Air Temperature over the North American Sector

WEINA GUAN,^{a,g} XIANAN JIANG,^{b,c,h} XUEJUAN REN,^{a,i} GANG CHEN,^{d,j} PU LIN,^{e,k} AND HAI LIN^{f,l}

^a CMA-NJU Joint Laboratory for Climate Prediction Studies, Institute for Climate and Global Change Research, School of Atmospheric Sciences, Nanjing University, Nanjing, China; ^b Joint Institute for Regional Earth System Science and Engineering, University of California, Los Angeles, Los Angeles, California; ^c Jet Propulsion Laboratory, California Institute of Technology, Pasadena, California; ^d Department of Atmospheric and Oceanic Sciences, University of California, Los Angeles, Los Angeles, California; ^e NOAA/Geophysical Fluid Dynamics Laboratory, Princeton, New Jersey; ^f Recherche en Prévision Numérique Atmosphérique, Environment and Climate Change Canada, Dorval, Quebec, Canada

(Manuscript received 12 February 2020, in final form 27 July 2020)

ABSTRACT: In this study, detailed characteristics of the leading intraseasonal variability mode of boreal winter surface air temperature (SAT) over the North American (NA) sector are investigated. This intraseasonal SAT mode, characterized by two anomalous centers with an opposite sign—one over central NA and another over east Siberia (ES)/Alaska—bears a great resemblance to the “warm Arctic–cold continent” pattern of the interannual SAT variability over NA. This intraseasonal SAT mode and associated circulation exert a pronounced influence on regional weather extremes, including precipitation over the northwest coast of NA, sea ice concentration over the Chukchi and Bering Seas, and extreme warm and cold events over the NA continent and Arctic region. Surface warming and cooling signals of the intraseasonal SAT mode are connected to temperature anomalies in a deep-tropospheric layer up to 300 hPa with a decreasing amplitude with altitude. Particularly, a coupling between the troposphere and stratosphere is found during evolution of the intraseasonal SAT variability, although whether the stratospheric processes are essential in sustaining the leading intraseasonal SAT mode is difficult to determine based on observations alone. Two origins of wave sources are identified in contributing to vertically propagating planetary waves near Alaska: one over ES/Alaska associated with local intraseasonal variability and another from the subtropical North Pacific via Rossby wave trains induced by tropical convective activity over the western Pacific, possibly associated with the Madden–Julian oscillation.


KEYWORDS: North America; Extreme events; Stratosphere–troposphere coupling; Surface temperature; Intraseasonal variability

1. Introduction

In the climate research community, a great interest has recently been developed in subseasonal predictions, with a forecast lead time ranging from two weeks to about one month (National Academies of Sciences, Engineering, and Medicine 2016; Vitart et al. 2017). Filling a gap between weather and seasonal climate predictions, subseasonal prediction provides important guidance for policy making and resource management for disaster mitigation purposes. For example, during

boreal winter, surface air temperature (SAT) exhibits pronounced intraseasonal variability over the mid- to high latitudes of the Northern Hemisphere (Lin and Brunet 2009; Lin 2015; Collow et al. 2019; Lin 2018; Stan and Krishnamurthy 2019; also see Fig. 1). These persistent SAT anomalies on the intraseasonal time scale can be closely related to regional extreme warm and cold episodes over North America (NA; e.g., Katz and Brown 1992), exerting significant influence on daily life, public health, energy, and so on. Improved understanding of the underlying physics regulating the intraseasonal SAT variability and skillful subseasonal prediction of SAT fluctuations, therefore, are of great social and economic importance (e.g., Lin 2018; Xiang et al. 2020; Lin 2020; Xiang et al. 2019).

As a dominant intraseasonal variability mode of tropical atmosphere, the Madden–Julian oscillation (MJO; Madden and Julian 1971) strongly influences not only tropical convective systems but also extratropical circulation and weather extremes via tropical convective-heating-induced planetary Rossby wave trains (Hoskins and Karoly 1981; Jin and Hoskins 1995; Stan et al. 2017), for example, by modulating the Pacific–North American (PNA) teleconnection pattern (Mori and Watanabe 2008; Johnson and Feldstein 2010; Riddle et al. 2013), the Arctic Oscillation (L’Heureux and Higgins 2008),

 Denotes content that is immediately available upon publication as open access.

^g ORCID: 0000-0003-3193-5477.

^h ORCID: 0000-0002-6010-0527.

ⁱ ORCID: 0000-0002-7137-4005.

^j ORCID: 0000-0003-4934-1909.

^k ORCID: 0000-0003-2577-6094.

^l ORCID: 0000-0003-4353-0426.

Corresponding author: Xianan Jiang, xianan@ucla.edu

DOI: 10.1175/JCLI-D-20-0096.1

© 2020 American Meteorological Society. For information regarding reuse of this content and general copyright information, consult the AMS Copyright Policy (www.ametsoc.org/PUBSReuseLicenses).

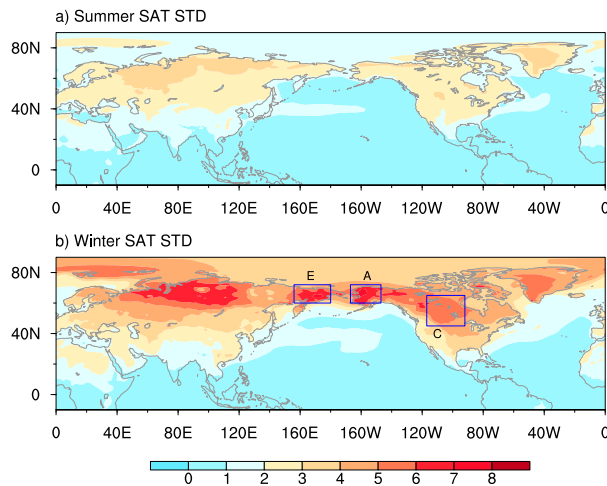


FIG. 1. Standard deviations of daily SAT anomalies ($^{\circ}\text{C}$) during (a) boreal summer (May–October) and (b) winter (November–March) from 1979 to 2017. The blue boxes E, A, and C in (b) denote the rough locations of ES, Alaska, and the central NA continent discussed in the text.

North Atlantic Oscillation (Cassou 2008; Lin et al. 2009), and also the polar vortex and sudden stratospheric warming events (Garfinkel and Schwartz 2017; Kang and Tziperman 2018b,a). It has been widely reported that the MJO has a profound influence on the intraseasonal SAT variability over NA (e.g., Vecchi and Bond 2004; Lin and Brunet 2009; Zhou et al. 2012; Baxter et al. 2014; Matsueda and Takaya 2015; Zheng et al. 2018; Riddle et al. 2013) and the Arctic region (e.g., Lee et al. 2011; Yoo et al. 2011, 2012a; Seo et al. 2016). In particular, the strongest winter SAT variability associated with the MJO is found over Alaska, Greenland, Siberia, the eastern United States, and southeastern Canada (Zheng et al. 2018).

The abovementioned observational studies thus suggest a critical role of the MJO as an important predictability source for subseasonal prediction over mid- to high latitudes. Improved subseasonal forecasts of extratropics indeed have been suggested in operational forecast systems when the errors associated with the representation of the MJO are reduced (Ferranti et al. 1990; Vitart and Molteni 2010; Riddle et al. 2013; Vitart 2014; Molteni et al. 2015). A recent study based on hindcasts from three operational models participating in the Seasonal-to-Subseasonal (S2S) Project (Vitart et al. 2017), however, indicated that predictive skill for the leading intraseasonal SAT mode over NA, identified by the first empirical orthogonal function (EOF) mode of pentad-mean boreal winter SAT anomalies, is independent from MJO status in the model initial conditions (Lin 2018). Xiang et al. (2019, 2020) also obtained a similar conclusion that the MJO does not significantly affect subseasonal prediction skill of the Northern Hemisphere extratropical SAT anomalies during boreal winter. The insignificant MJO impact on subseasonal predictions of extratropical SAT in the above studies, however, could possibly be due to model deficiencies in representing the MJO convection-induced teleconnection patterns in climate and weather forecasting models

(e.g., Henderson et al. 2017; Wang et al. 2020). By conducting a wave activity flux analysis, Lin (2018) further suggested that the energy source for the leading intraseasonal SAT mode over NA could originate over the North Pacific and is independent from tropical convective activity associated with the MJO.

While the dominant intraseasonal SAT pattern over NA has been previously examined (Lin 2015, 2018), its detailed vertical structures and evolution characteristics have not been extensively investigated. Meanwhile, physical mechanisms of the intraseasonal SAT variability over NA also remain elusive. In this study, we explore three-dimensional structures in temperature and circulation anomalies associated with the leading intraseasonal SAT variability mode over the NA sector as well as its impact on regional weather extremes. Considering previous studies on the importance of stratospheric planetary wave reflection on the amplification of tropospheric blocking (e.g., Kodera et al. 2013, 2016; Kidston et al. 2015), a particular interest of this study is to explore a plausible role of stratosphere–troposphere coupling during evolution of the intraseasonal SAT variability mode.

The remainder of this paper is organized as follows: Section 2 introduces the data and methods used in this study. Section 3 examines basic features of the leading mode of the intraseasonal SAT variability over the NA sector. The precipitation, sea ice, and extreme warm/cold events related to this mode are presented in section 4. Detailed vertical structures in temperature, moisture, and circulation in both the troposphere and stratosphere associated with this intraseasonal SAT mode are further examined in section 5. Particularly, a plausible role of the stratospheric processes on the intraseasonal SAT variability mode is explored. Finally, a summary and discussions are given in section 6.

2. Data and methods

Daily data from the European Centre for Medium-Range Weather Forecasts (ECMWF) interim reanalysis (ERA-Interim) are used for this study (Dee et al. 2011). The variables include SAT at 2-m height, 3D geopotential height (Z), zonal and meridional winds (u, v), temperature (T), and specific humidity (q) with a spatial resolution of $0.75^{\circ} \times 0.75^{\circ}$ and 37 vertical levels during 1979–2017. Daily 1° global precipitation data from the Global Precipitation Climatology Project (GPCP) Climate Data Record (CDR, version 1.3; Adler et al. 2017) from 1996 to 2017 is used to characterize precipitation anomalies associated with the leading intraseasonal SAT mode. Also analyzed in this study are daily passive microwave sea ice concentration (SIC) data, version 3, from the National Snow and Ice Data Center (NSIDC; Peng et al. 2013), which are on $25\text{ km} \times 25\text{ km}$ horizontal grids and cover the period of 1988–2017.

Daily intraseasonal anomalies of each variable are obtained by first removing the climatological annual cycle (annual mean plus three leading harmonics) and then a 10–90-day bandpass filtering. If not particularly mentioned, all analyses in the following will be conducted for the extended boreal winter season from November to March.

3. The leading intraseasonal SAT variability mode over NA

Standard deviations of 10–90-day-filtered SAT anomalies during boreal summer and winter are illustrated in Fig. 1. While

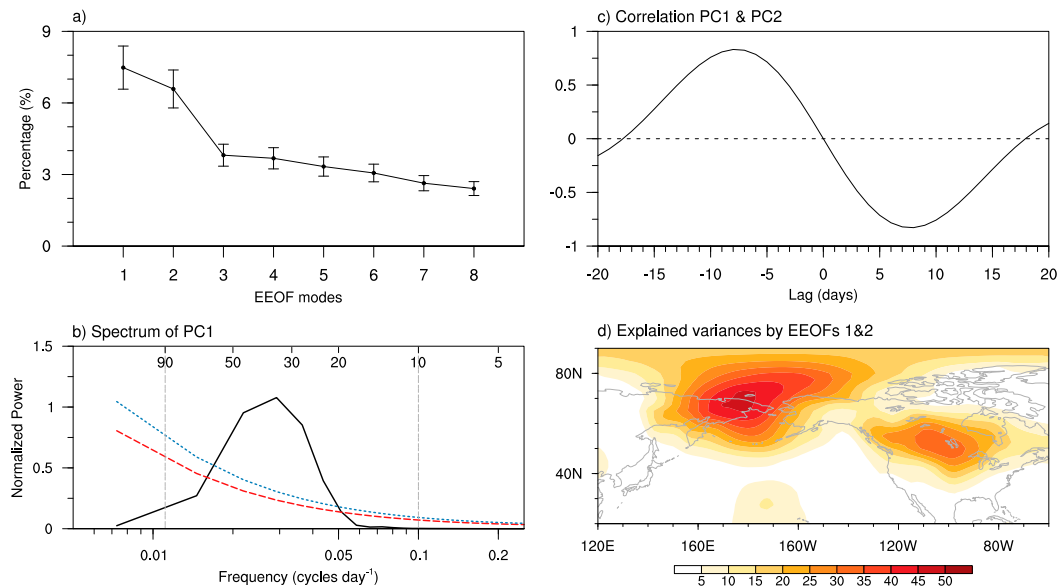


FIG. 2. (a) Percentages of variances explained by the first eight leading EEOF modes. Error bars are calculated based on North et al. (1982). (b) Power spectra of PC₁ in winters from 1979 to 2017 (black), with Markov red noise spectrum (red) and the 95% confidence level (blue). (c) Lag correlations between PC₁ and PC₂. A positive (negative) lag denotes PC₂ leading (lagging) PC₁. (d) Spatial distribution of percentages of local variances of 10–90-day SAT anomalies explained by the EEOF₁ and EEOF₂.

intraseasonal SAT variability over the Northern Hemisphere is rather weak during boreal summer in general, pronounced intraseasonal variability is found over mid- to high-latitude land regions during boreal winter, with active centers over west Siberia, east Siberia (ES), the NA continent with a local maximum over Alaska, and part of the polar region including Iceland, with maximum standard deviations exceeding 6°C. These standard deviation patterns of the intraseasonal SAT anomalies during both summer and winter largely resemble those derived by the monthly mean SAT anomalies (Trenberth and Shea 2005). Causes for the strong intraseasonal SAT variability over the above areas during boreal winter are not fully understood, although the winter mean state such as a strong meridional gradient in climatological surface temperature due to land–ocean contrast over mid- to high latitudes and land–atmosphere interactions are considered to play an important role considering the prevalence of strong variability over land during boreal winter. In this study, we will focus on the intraseasonal SAT variability during boreal winter over the extended NA sector, including Alaska, Canada, the contiguous United States, ES, and the neighboring North Pacific and Arctic regions, which is referred to as NA in the following discussions for the sake of brevity if not specifically mentioned.

Instead of the EOF analyses used in previous studies (e.g., Lin 2015, 2018), we employ an extended EOF (EEOF) analysis (Weare and Nastrom 1982; Jiang and Waliser 2009) of 10–90-day-filtered SAT anomalies during 1979–2017 winters to identify the dominant intraseasonal SAT variability mode over the NA sector. (The 1979 winter represents the period from 1 November 1979 to 31 March 1980, and so on.) The EEOF analysis is conducted over the region of 20°–90°N, 120°E–60°W (see Fig. 3)

with a time lag of 31 days. The EEOF is essentially the same as the EOF just using an extended covariance matrix with the daily data during all these time lags. The derived eigenvectors based on the EEOF analysis therefore contain a series of evolution patterns of the leading modes. As shown in Fig. 2a, the first and second modes (EEOF₁ and EEOF₂), which are in quadrature to each other, are not separable based on the criteria of North et al. (1982), and thus represent the same leading intraseasonal SAT mode. The first two EEOF modes account for 7.5% and 6.6% of the total intraseasonal SAT variance, respectively. As suggested by power spectra of PC₁ (Fig. 2b), this leading intraseasonal mode exhibits a prevailing period of 20–50 days. Lead–lag correlations between PC₁ and PC₂ (Fig. 2c) further suggest that PC₁ leads PC₂ by about 8 days, and negative PC₁ lags PC₂ by 8 days, suggesting a period of about 32 days associated with this leading intraseasonal SAT mode, consistent with the period corresponding to the peak spectrum in Fig. 2b.¹ Estimated by correlations between daily time series of 10–90-day-filtered SAT anomalies and anomalies reconstructed using the EEOF₁ and EEOF₂, the leading intraseasonal SAT modes explain up to about 50% of daily intraseasonal SAT variations, particularly over ES/Alaska and central NA (Fig. 2d).

Evolution of the leading intraseasonal SAT mode is presented in Fig. 3 based on lag regressions of 10–90-day-filtered SAT anomalies onto PC₁ from days –12 to 9 at a 3-day interval. This leading intraseasonal SAT mode consists of two

¹ Note that the period of the derived leading modes is not sensitive to the time lag used for the EEOF. Using a time lag of 41 days for the EEOF analysis, for example, will yield a similar leading intraseasonal mode with a dominant period of 32 days.

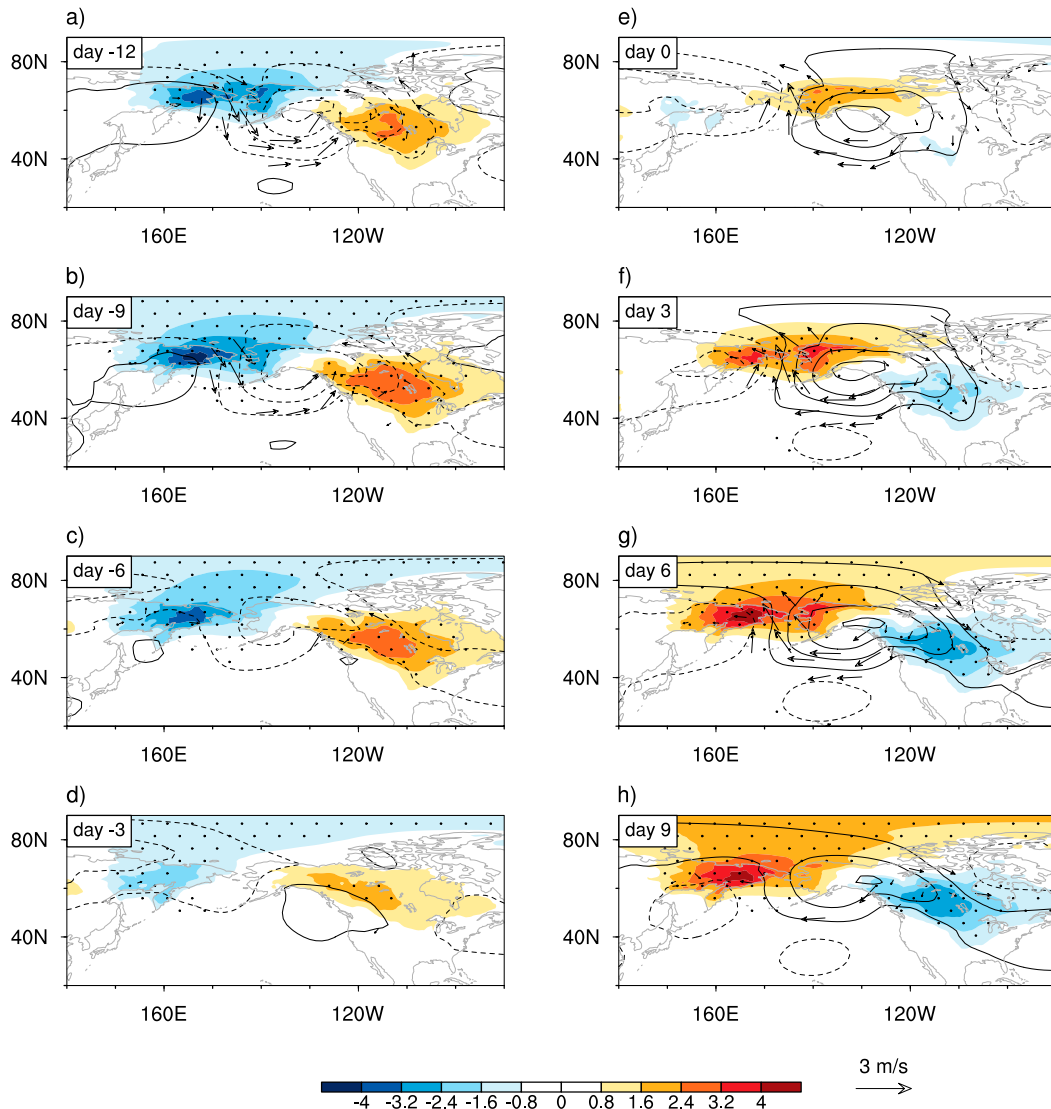


FIG. 3. Lag regressions of anomalous SAT ($^{\circ}\text{C}$; shading), SLP (contours with an interval of 1.5 hPa, dashed if negative; zero contours omitted), and 10-m winds (m s^{-1} ; black vectors; plotted only for areas surpassing the 95% significance level) onto the normalized PC_1 from (a) day -12 to (h) day 9 with an interval of 3 days. Areas with black dots indicate SAT anomalies surpassing the 95% significance level.

anomalous centers with opposite signs: one over ES/Alaska with anomalies spreading over a large area of the Arctic region and another center with an opposite sign over central NA to the east of Canadian Rockies. At day -12 , the anomalous SAT pattern is characterized by warm anomalies over Canada and the northern United States and cold anomalies over ES/Alaska (Fig. 3a). Both warm and cold SAT anomalies intensify at day -9 (Fig. 3b). They start to weaken from day -9 to day -3 (Figs. 3b–d) and shift westward from day -3 to day 0 (Figs. 3d,e). At day 0, weak positive SAT anomalies are found over Alaska (Fig. 3e). In the following days, positive SAT anomalies gradually develop over ES/Alaska on both sides of the Bering Strait, and negative SAT anomalies over the central NA continent (Figs. 3f–h). The SAT anomalous pattern at day

3 largely mirrors that at day -12 with an opposite sign, further suggesting a period of about 30 days of the leading intra-seasonal SAT mode.

Note that cold SAT anomalies over ES/Alaska and warm anomalies over central NA from day -12 to day -6 are coupled with an anomalous surface low near Alaska (Figs. 3a–c). As a result, cold SAT anomalies over ES/Alaska can be largely due to cold temperature advection by the northerly anomalous winds, while warm SAT anomalies over the NA continent due to warm temperature advection by southwesterly anomalous winds associated with the low pressure system, as previously noted (e.g., Lin 2018; Martineau et al. 2017; Guan et al. 2020). It is also worth noting that the maximum amplitude of the anomalous low and associated winds is observed at day -12 ,

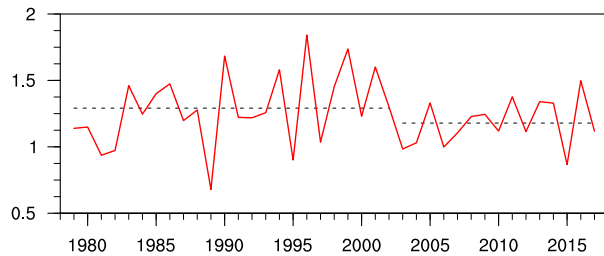


FIG. 4. Time series of winter mean amplitude of the intraseasonal SAT variability defined by $\sqrt{PC1^2 + PC2^2}$. The black dashed lines indicate the average amplitude for the two periods of 1979–2002 and 2003–17.

which leads the maximum amplitude in warm and cold anomalies (day -9), further suggesting that SAT anomalies tend to be driven by atmospheric circulation. An opposite case is found during the period from day 3 to day 9, that is, positive SAT anomalies over ES/Alaska and negative SAT anomalies over NA are associated with an anomalous surface high (Figs. 3f–h). In the following discussions, the period when strong negative (positive) SAT anomalies are present over ES/Alaska (central NA), that is, day -12 to -6 , is referred to as the negative phase of the intraseasonal SAT mode; and the period corresponding to strong SAT anomalies with an opposite sign over the above two regions, that is, days 3 to 9, is defined as the positive phase, and the period in between, that is, days -3 and 0, as the transition phase of the intraseasonal SAT mode.

This leading intraseasonal SAT mode based on the EEOF as shown in Fig. 3 is largely similar to those previously identified based on EOF analyses of 5-day mean SAT anomalies over the Northern Hemisphere between 20° and 80°N (Lin 2018) and over the NA continent (Lin 2015); their EOF₁ modes largely resemble the anomalous SAT pattern at day -9 in Fig. 3. However, the PCs associated with the EOF₁ modes in the previous studies exhibit a main spectral peak around 50 days and a secondary peak around 30 days (e.g., Fig. 3 in Lin 2015). The lower-frequency intraseasonal periodicity of extratropical variability has also been previously reported (e.g., Ghil and Mo 1991; Plaut and Vautard 1994; Johnson and Feldstein 2010; Stan and Krishnamurthy 2019). Our analysis suggests that the leading intraseasonal SAT modes with both the higher (e.g., 10–40 days) and lower frequencies (e.g., 40–70 days) share similar spatial patterns as shown in Fig. 3 (not shown). Therefore, the regression patterns using the PC₁ based on the EOF analysis as in the previous studies may represent mixed features of the intraseasonal SAT variability modes with slightly different periodicity. In this study, due to more strict constraints of the EEOF method by including evolution of SAT anomalies at different time lags, the mode with a period of about 32 days is identified as the leading mode.

It is also noteworthy that the spatial pattern of the leading intraseasonal SAT mode shown in Fig. 3 largely resembles the “warm-Arctic–cold-continent” (WACC) pattern over the NA sector that has been observed in SAT trend in recent decades (e.g., Cohen et al. 2014; Kug et al. 2015; Sigmond and Fyfe 2016; Sun et al. 2016; Clark and Lee 2019), and particularly that

associated with the interannual SAT variability during boreal winter (Kug et al. 2015; Blackport et al. 2019; Guan et al. 2020). In this regard, the WACC-type intraseasonal SAT variability mode shown in Fig. 3 tends to serve as a building block for the prevailing SAT variability over NA on interannual time scales (e.g., Guan et al. 2020). Understanding of mechanisms regulating the leading intraseasonal SAT variability mode is therefore critical for improved understanding of the lower-frequency variability and long-term trend of SAT over NA and the Arctic region.

Some recent studies reported weakened intraseasonal SAT variability over NA in the most recent decades (e.g., Screen 2014; Collow et al. 2019), which is supported by interannual variations of the amplitude of the leading intraseasonal SAT mode during 1979–2017 winters (Fig. 4). Here, the amplitude of the leading intraseasonal SAT mode during each winter is derived by averaging their corresponding daily values based on the two leading PCs with $\sqrt{PC1^2 + PC2^2}$. The weaker amplitude of the intraseasonal SAT variability after 2002 is readily seen in Fig. 4 with average amplitudes of 1.25 and 1.1 for the period of 1990–2002 and 2003–17, respectively, which is statistically significant at the 90% level, although the underlying physics needs to be further investigated. Collow et al. (2019) ascribed the general reduction of intraseasonal SAT activity over NA to the weakened latitudinal temperature gradient associated with the Arctic sea ice loss in recent decades. Screen (2014), on the other hand, hypothesized that the significantly decreased subseasonal cold-season temperature variability over the Northern Hemisphere mid- to high latitudes in recent decades is associated with more rapidly warming of cold days with northerly winds than warming days with southerly winds.

4. Modulation of the leading intraseasonal SAT mode on weather extremes

In this section, the influence of the leading intraseasonal SAT mode on sea ice and precipitation anomalies as well as the occurrence frequency of extreme warm and cold events is examined.

Figure 5 shows lag regressions of 10–90-day-filtered SIC anomalies onto the normalized PC corresponding to the EEOF₁ over the Chukchi and Bering Seas (CBS) where the strongest SIC anomalies are observed. Considering about 40% of climatological SIC over CBS, the intraseasonal sea ice anomalies associated with the leading SAT mode (i.e., $\pm 4\%$) can reach 20% of the local climatological values. Associated with the cold SAT anomalies over ES/Alaska from day -12 to day -3 (Figs. 3a–d), positive SIC anomalies are observed over CBS (Figs. 5a–d). During the transition period of the local SAT anomalies over ES/Alaska from negative to positive after day 0 (Fig. 3e), SIC anomalies gradually become negative after day 3 over CBS (Fig. 5f) and intensify in the following days (Figs. 5g–i). Note that the maximum SIC anomalies over CBS are observed at day -6 (Fig. 5c), while the local minimum SAT anomalies near day -9 (Fig. 3b), slightly leading positive SIC anomalies. Similarly, the maximum warming over ES/Alaska at day 6 (Fig. 3g) also leads the peak of negative SIC anomalies between days 9 and 12 (Figs. 5h,i). This lead-lag relationship between SAT and SIC anomalies averaged over CBS (the blue box in Fig. 5c) is clearly illustrated in Fig. 6. Since SAT warming anomalies over CBS lag the local surface southerly wind

Sea ice anomalies regressed on PC1

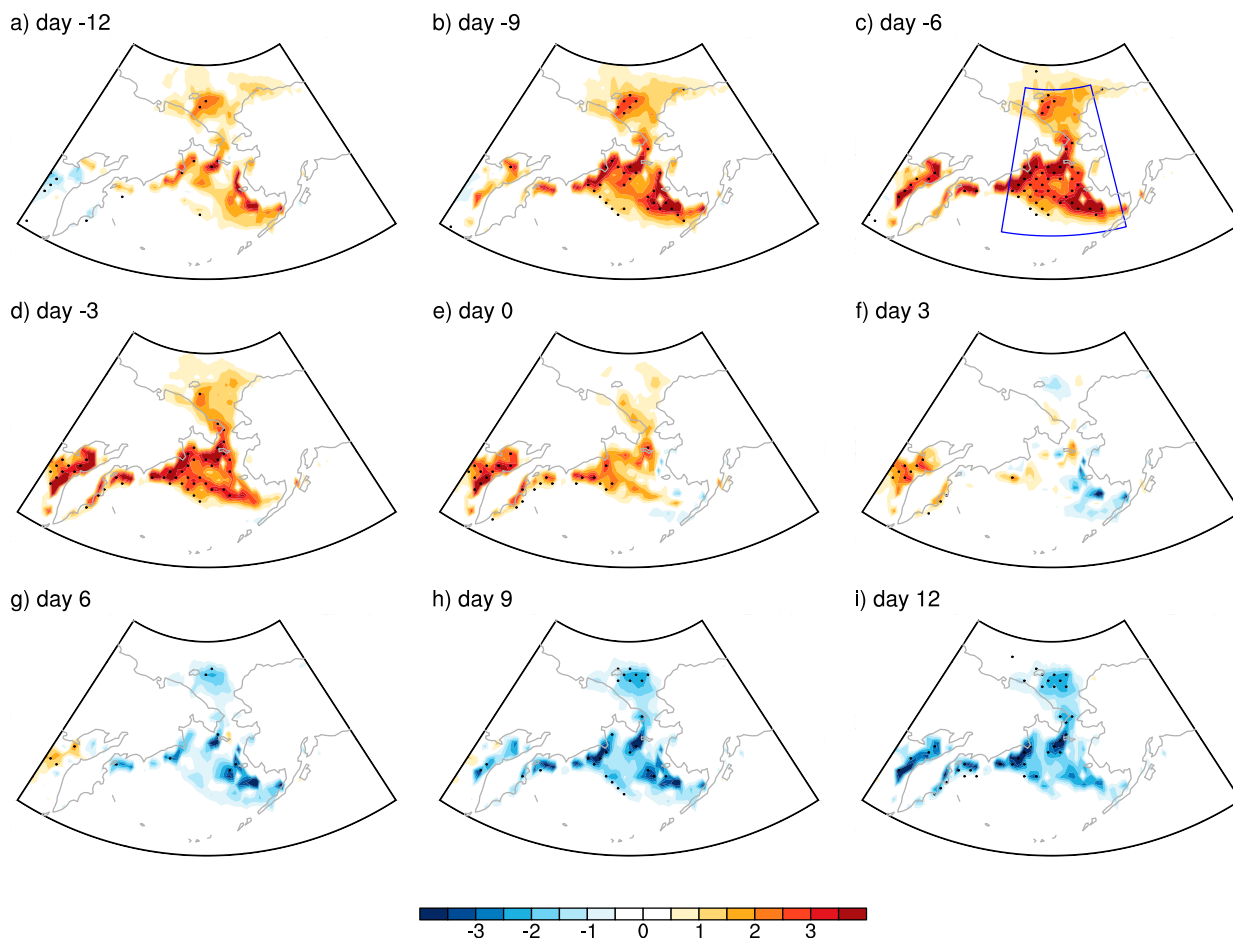


FIG. 5. Lag regressions of intraseasonal sea ice anomalies (%) onto the normalized PC₁ from (a) day -12 to (i) day 12 . The black dots denote the areas where anomalies are statistically significant at the 95% confidence level. The blue box in (c) indicates the CBS region (55° – 72° N, 175° E– 160° W).

anomalies associated with anomalous anticyclonic circulation over Alaska as discussed in Fig. 3, these results thus suggest a critical role of atmospheric circulation in driving the SAT warming and sea ice loss over the CBS region. For example, as previously reported (e.g., Lin and Derome 1995; Yoo et al. 2012b; Flournoy et al. 2016; Park et al. 2015), the southerly surface wind anomalies can lead to enhanced column water vapor (to be shown in Fig. 11b) through temperature and moisture advection, which will further lead to enhanced downward longwave radiation (DLWR) and thus surface warming. Meanwhile, the southerly anomalous winds can also reduce surface turbulent heat flux (THF) by weakening the northerly seasonal mean winds over CBS (Guan et al. 2020), which also contributes to local surface warming. The important role of DLWR and THF anomalies for surface warming over CBS associated with the leading intraseasonal SAT mode is further supported by Fig. 6. Namely, enhanced DLWR and reduced THF slightly lead CBS warming by 1–2 days, while CBS sea ice

reduction lags the SAT maximum by about 5 days, largely in agreement with that recently reported in Guan et al. (2020), which is based on unfiltered daily anomalous fields.

Figure 7 shows the lag-regressed patterns of precipitation anomalies against the normalized PC₁ along with 200-hPa Z anomalies. Large anomalous rainfall signals associated with the leading intraseasonal SAT mode are found over the northwest coast of NA, ES/Alaska, the central Pacific near Hawaii, and tropical oceans near the Maritime Continent/western Pacific. Northwestward migration of enhanced rainfall anomalies is observed along the northwest coast of NA during the negative phase of the intraseasonal SAT variability, that is, day -12 to day -6 , in conjunction with cyclonic circulation at 200 hPa centered near ES/Alaska (Figs. 7a–c). This cyclonic circulation is a part of the west Pacific (WP)-like teleconnection pattern extending from the central subtropical Pacific to mid- to high latitudes (Wallace and Gutzler 1981; Baxter and Nigam 2015). Meanwhile, weak negative rainfall anomalies

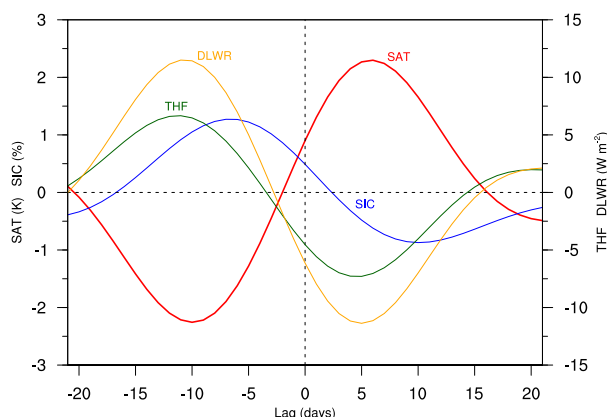


FIG. 6. Evolution of the SAT index and various fields averaged over CBS (55°–72°N, 175°E–160°W; blue box in Fig. 5c) based on lag regressions onto the normalized PC₁. Positive values in THF and DLWR represent upward fluxes.

start to appear over northwest coast of the United States at day −6 (Fig. 7c), and then intensify and experience a similar northwestward movement along the coastline as the positive rainfall phase in earlier days. Negative rainfall anomalies over the northwest NA coast reach its maximum amplitude at day 3 (Fig. 7f). Rainfall anomalies over the central Pacific near the Hawaiian Islands and ES/Alaska are largely in an opposite sign with major rainfall anomalies over the west coast of NA.

It has been previously proposed that the intraseasonal SAT variability over the mid- to high latitude can be traced back to variability in tropical convection via diabatic-heating-induced Rossby wave teleconnection pattern, for example, associated with the MJO (Yoo et al. 2011; Flourenoy et al. 2016; Zheng et al. 2018; Hu et al. 2019), or enhanced convection in the tropical central Pacific due to low-level convergence originated from the East Asian cold surge (Lin 2015). Plausible connection between the leading intraseasonal SAT mode and tropical convective activity is examined in Fig. 8 by displaying the longitude–time evolution of precipitation anomalies along the equator derived by lag regressions of precipitation anomalies averaged over 15°S–15°N onto PC₁. Note that the eastward-propagation signals from the Indian Ocean to the western Pacific of the MJO are clearly discerned in Fig. 8, suggesting that the leading intraseasonal SAT mode over NA could be associated with the eastward-propagating MJO mode. It is shown in Fig. 7 that associated with the slow eastward movement of enhanced convection from the Maritime Continent to the western Pacific from day −12 to 0, a westward migration of anomalous high at 200 hPa over the central Pacific near 30°N can be observed. This may indicate that significant convective activity near the Maritime Continent/western Pacific can play a role in forming the WP-like teleconnection pattern associated with evolution of the leading intraseasonal SAT, although further investigations are needed to elaborate the underlying processes.

To examine the impact of the leading intraseasonal SAT mode on regional extreme warm and cold events, a complete evolution cycle of the leading intraseasonal SAT mode is separated into eight phases based on the time series of PC₁ and

PC₂, following an approach used for the MJO (Wheeler and Hendon 2004). Days with strong SAT variability over NA can be identified by daily SAT amplitudes ($\sqrt{PC_1^2 + PC_2^2} \geq 1$) greater than 1. Composite SAT anomalies during the eight phases of the intraseasonal SAT mode can then be obtained by averaging the 10–90-day-filtered SAT anomalies over selected strong SAT days (Fig. 9). During phases 1 and 8 (Fig. 9a), strong warm (cold) anomalies are located over NA (ES/Alaska), which weaken and move westward in phases 2 and 3 (Fig. 9b) and eventually transit to an opposite phase during phases 4 and 5 (Fig. 9c).

Cold and warm extreme days at each grid during November–March from 1979 to 2017 are then identified using daily SAT anomalies. A cold extreme on a particular day is identified if the SAT anomalies fall below the 10th-percentile threshold value during the all-5-day period centered on that day. Similarly, a warm extreme is defined by SAT anomalies exceeding the 90th-percentile threshold value. Distributions of the warm and cold extreme days during different phases of the leading SAT mode are displayed in Fig. 9. Frequent occurrence of extreme cold days over the Arctic region and western Canada is largely observed during phases 1 and 8 and phases 4 and 5, respectively (Figs. 9e,g); while extreme warm days occur over north Canada during phase 1 and 8 (Fig. 9i) and near the ES/Alaska region during phases 4 and 5 (Fig. 9k), largely in accord with anomalous cold and warm SAT patterns of the intraseasonal SAT mode.

To summarize, analyses in this section illustrate that the leading intraseasonal SAT mode over NA is closely associated with regional extreme weather events, including precipitation over the northwest coast of NA, sea ice over CBS, and extreme warm and cold events over the NA continent and the Arctic region. Therefore, considering its extended-range prediction skill (e.g., Lin 2018), this intraseasonal SAT mode can provide an important predictability source for subseasonal predictions of regional extreme weather activity over the NA sector.

5. Vertical structure of the leading intraseasonal SAT mode and role of the stratosphere–troposphere coupling

In this section, vertical structure of the leading intraseasonal SAT mode is further explored to gain insight into physical mechanisms regulating this intraseasonal mode. Figure 10 illustrates spatial patterns of regressed T and Z anomalies onto PC₁ at day −9 and day 0, representing the negative phase of the intraseasonal SAT mode with maximum warm (cold) SAT anomalies over central NA (ES/Alaska) and the transition phase with surface warming over Alaska, respectively (Fig. 3). An equivalent barotropic structure in vertical T and Z anomalies is clearly evident in the troposphere. For example, at day −9, in accord with anomalous SAT pattern in Fig. 3b, negative (positive) T anomalies over ES/Alaska (central NA) and the accompanying low (high) system over Alaska (north Canada) can be discerned in vertical levels up to 300 hPa. In contrast to regional features in anomalous T and Z patterns in the lower troposphere (Fig. 10e), circulation and associated T anomalies in the stratosphere above 100 hPa are largely characterized by the zonal-wavenumber-1 pattern (Figs. 10a,b),

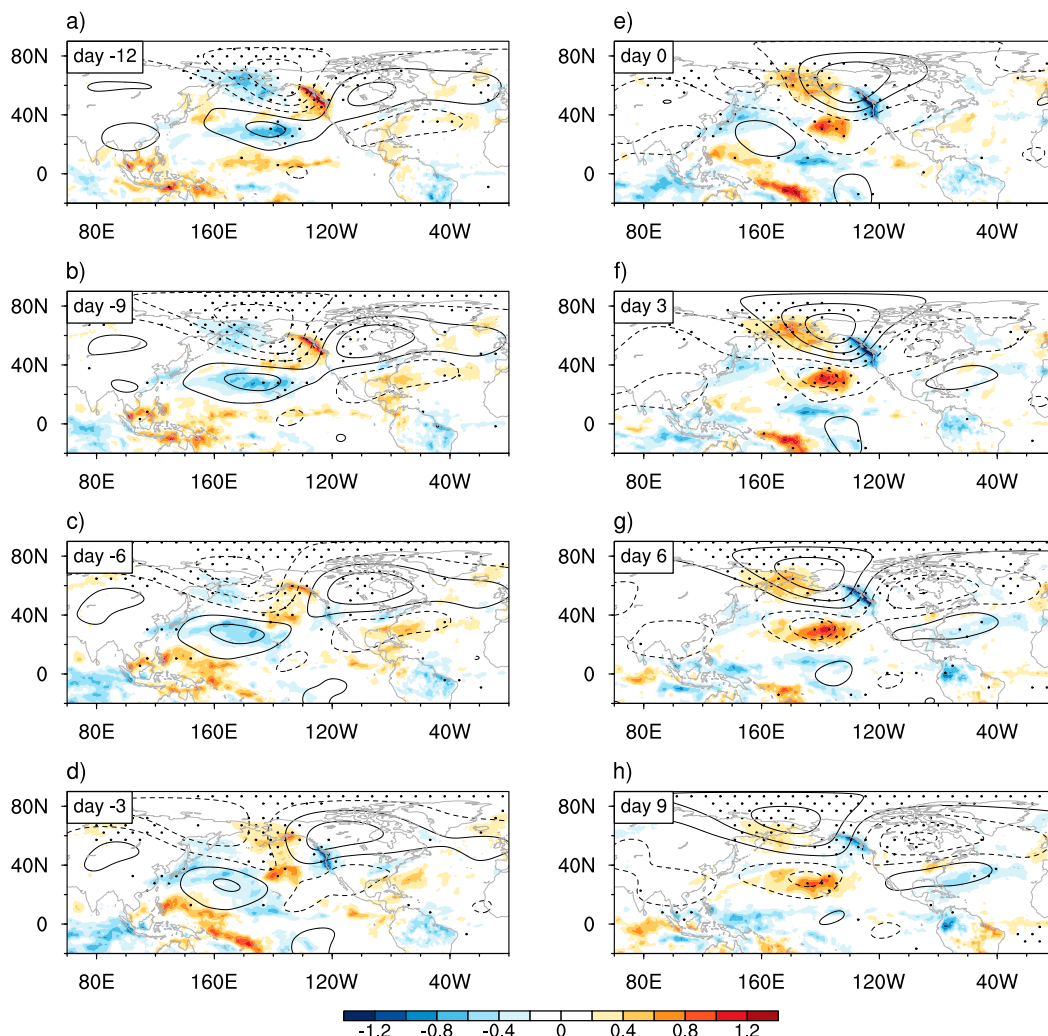


FIG. 7. As in Fig. 3, but for anomalous precipitation (mm day^{-1} ; shading) and the 200-hPa streamfunction (contours with an interval of $2 \times 10^6 \text{ m}^2 \text{ s}^{-1}$, dashed if negative; zero contours omitted). The black dots denote the regressed precipitation anomalies that are statistically significant at 95% confidence level.

possibly due to the blocking of the upward propagation of synoptic-scale waves by the strong westerly polar night jet (Charney and Drazin 1961). As a result, both cyclonic anomalies in Z and negative T anomalies exhibit westward shift above 100 hPa (Figs. 10a,b), a typical signature of upward planetary wave propagation. Largely similar features in the stratosphere are also seen at day 0, for example, corresponding to surface warming over Alaska, a large area of anomalous warming is discerned at 10 hPa in mid- to high latitudes with a maximum over Siberia near 120°E (Fig. 10f). The regressed T and Z anomalies during the positive phase of the intraseasonal SAT mode are largely similar to those during the negative phase but with an opposite sign (figure not shown).

Figure 11 further presents time–pressure profiles of lag-regressed anomalous T and q over ES/Alaska ($60^\circ\text{--}70^\circ\text{N}$, $160^\circ\text{E}\text{--}160^\circ\text{W}$) and Z near the Alaska region ($50^\circ\text{--}70^\circ\text{N}$, $180^\circ\text{--}120^\circ\text{W}$) against PC_1 . Selection of the two different regions for T and Z are mainly due to the spatial phase difference between

these two fields (Fig. 3). As shown in Fig. 11a, associated with negative SAT anomalies over the ES/Alaska region before day -3 , negative T anomalies are also observed in the troposphere up to about 300 hPa, with the maximum amplitude near the surface. Similarly, positive T anomalies are also found in the mid- and upper troposphere after day 0 associated with surface warming over ES/Alaska. Anomalous T signals associated with the leading intraseasonal SAT mode are also seen in the stratosphere above 50 hPa, with the maximum positive T anomalies leading surface warming by about 10 days. On the other hand, reduced (enhanced) moisture in the lower troposphere is found to be coupled with tropospheric and surface cooling (warming) anomalies (Fig. 11b), which could result from similar horizontal advection processes by the cyclonic (anticyclonic) circulation near Alaska (Fig. 3). As previously discussed, enhanced (reduced) low-level moisture could enhance the surface warming (cooling) effect through increased (decreased) DLWR (e.g., Yoo

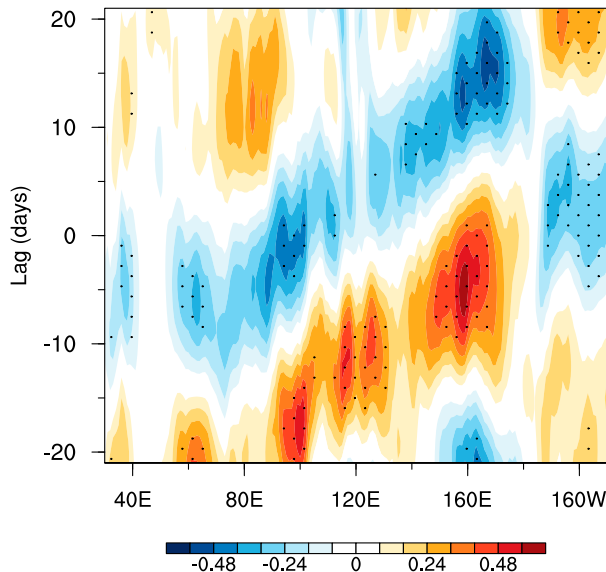


FIG. 8. Longitude–time evolution of latitude-averaged (10°S – 10°N) precipitation anomalies (mm day^{-1}), which are derived by lag regressions onto the normalized PC_1 . The black dots denote the areas that are statistically significant at the 95% confidence level.

et al. 2012b; Flournoy et al. 2016; Graversen et al. 2008; Screen and Simmonds 2010).

Note that the positive equivalent barotropic Z anomalies near Alaska after day 0 in the troposphere, which are responsible for low-level warming anomalies over ES/Alaska via associated anticyclonic circulation (Figs. 3e–h), are found to be closely linked to signals in the stratosphere (Fig. 11c). This linkage between Z anomalies in the stratosphere and troposphere could result from the westward tilt in Z anomalies with height as discussed in Fig. 10 and the westward movement of the intraseasonal SAT mode. Due to the relatively low density, the strongest Z anomalies are discerned in the stratosphere. The peak of warm SAT anomalies over ES/Alaska tends to lag positive Z anomalies in the stratosphere near Alaska by about one week (cf. Figs. 11a,c). This result, therefore, suggests that the intraseasonal Z anomalies in the stratosphere near Alaska can be used as a useful precursor for prediction of the intraseasonal SAT variability over the NA sector.

A strong coupling between the troposphere and stratosphere is further illustrated by examining evolution of the amplitude in zonal-wavenumber-1 structure of the lag-regressed Z anomalies (averaged over 50° – 70°N) as a function of vertical pressure (Fig. 11d). Selection of zonal-wavenumber-1 structure is mainly based on the consideration that the longest planetary waves are prone to propagate upward into the stratosphere. Figure 11d clearly illustrates that during both positive and negative phases of the leading SAT mode, gradual upward propagation of the amplitude of wavenumber-1 Z anomalies, that is, energy propagation, is found from the midtroposphere around 500 hPa all the way into the stratosphere, suggesting a critical role of the troposphere in driving stratospheric wave activity. This will be further discussed in the following.

Detailed evolution features in 500 hPa Z anomalies associated with the leading intraseasonal SAT mode is further shown in Fig. 12. Associated with strong cold (warm) anomalies over

ES/Alaska (central NA) at days -12 and -9 , a low pressure system at 500 hPa is located over Alaska region and an anomalous high near Hudson Bay over Canada. In the following days, both the anomalous high and low weaken and shift westward, associated with the transition phase of the intraseasonal SAT mode. At day 0, the anomalous high arrives over Alaska (Fig. 12e); meanwhile, a new anomalous low starts to emerge over the Hudson Bay area. After day 3, rapid intensification of the high and low over Alaska and Hudson Bay, respectively, leads to strong positive SAT anomalies over ES/Alaska, and negative anomalies over central NA. These results suggest that evolution of the leading intraseasonal SAT mode over NA is closely associated with an oscillatory northwest–southeast dipole of anomalous low and high systems in the troposphere, with one located near Alaska, and another near Hudson Bay in Canada. The anomalous Z pattern at 500 hPa associated with the intraseasonal SAT mode as shown in Fig. 12 resembles the WP-like teleconnection pattern (e.g., Tanaka et al. 2016; Baxter and Nigam 2015; Linkin and Nigam 2008; Dai and Tan 2019) and the Alaskan Ridge regime (Casola and Wallace 2007; Straus et al. 2007; Carrera et al. 2004). Also note that westward displacement of intraseasonal disturbances over Alaska and the CBS region has also been previously reported as the retrograding low-frequency waves (e.g., Kushnir 1987).

Figure 13 further illustrates evolution of Z anomalies at 5 hPa associated with the leading intraseasonal SAT mode. A global wavenumber-1 pattern is clearly discerned in Z anomalies at 5 hPa, which represents variability associated with displacement of the stratospheric polar vortex. The Z anomalies are relatively weak at day -12 , and then quickly develop into a dipole pattern with a positive center over north Canada and a negative one over the Eurasian continent (Figs. 13b–d), coincident with the negative phase of the intraseasonal SAT mode. After day 0, accompanying the transition period of anomalous SAT, negative Z anomalies over Eurasia quickly weaken; meanwhile, positive anomalies shift westward toward the Eurasian continent. A dipole pattern in Z anomalies reemerges after day 6 with an opposite sign to that during day -9 to day -3 , associated with the positive phase of the intraseasonal SAT mode. As shown in Fig. 11d and to be further discussed below, the establishment of the wavenumber-1 dipole patterns in Z anomalies at 5 hPa is closely linked to upward propagation of planetary waves from the troposphere.

Next, an analysis of the 3D wave activity flux (WAF) is conducted to explore a possible role of the stratosphere associated with evolution of the leading intraseasonal SAT mode. The calculation of 3D WAF is based on the \mathbf{W} vector following Takaya and Nakamura (2001), which is expressed as

$$\mathbf{W} = \frac{P}{2|\mathbf{U}|} \left\{ \begin{array}{l} U(\psi_x'^2 - \psi'\psi_{xx}') + V(\psi_x'\psi_y' - \psi'\psi_{xy}') \\ U(\psi_x'\psi_y' - \psi'\psi_{xy}') + V(\psi_y'^2 - \psi'\psi_{yy}') \\ \frac{f_0^2}{N^2} [U(\psi_x'\psi_z' - \psi'\psi_{xz}') + V(\psi_y'\psi_z' - \psi'\psi_{yz}')] \end{array} \right\},$$

where ψ' is the perturbation streamfunction (ψ), derived based on lag regressions of 10–90-day-filtered ψ against the PC_1 of the

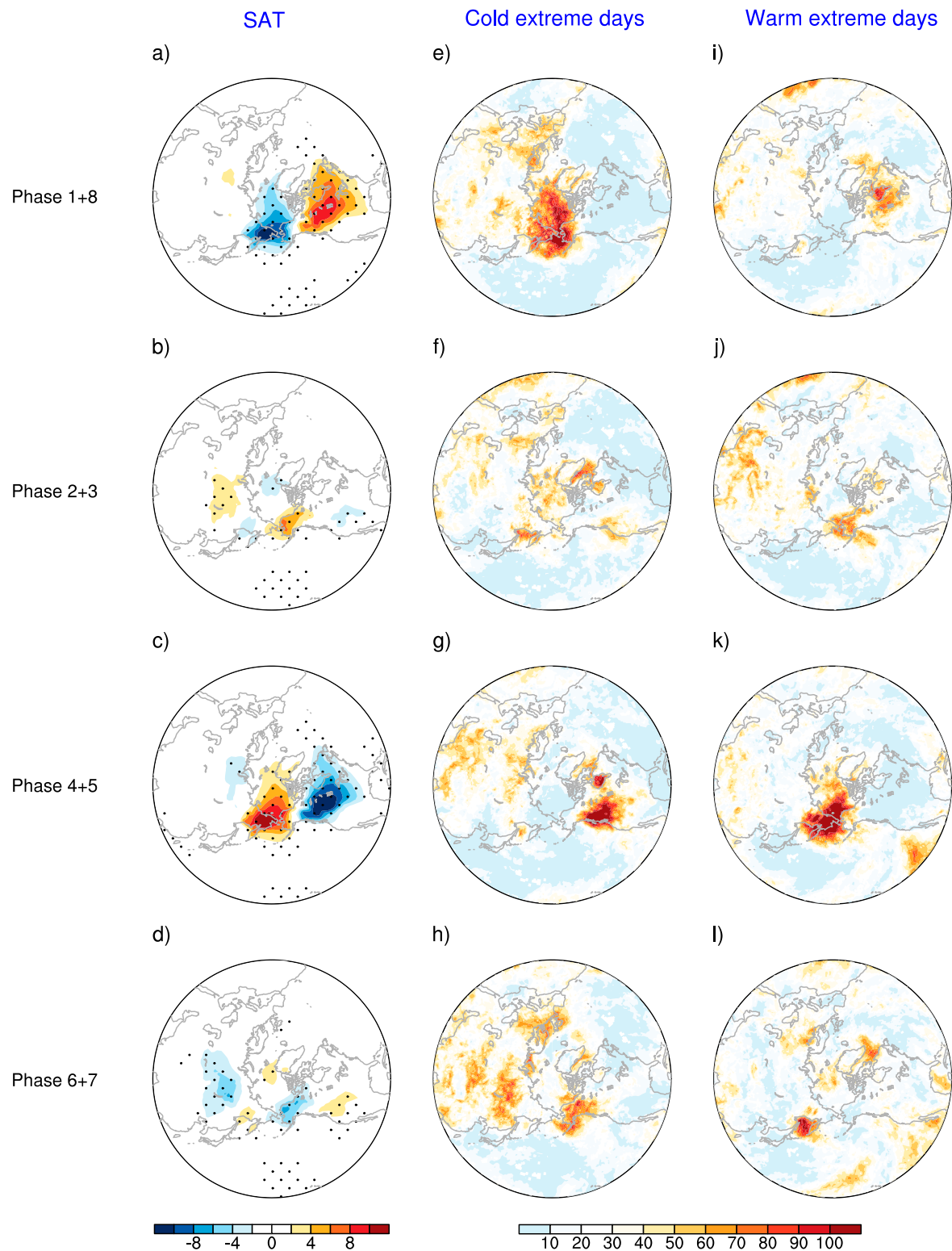


FIG. 9. (a)–(d) Composite SAT anomalies ($^{\circ}\text{C}$), and the distribution of the (e)–(h) cold and (i)–(l) warm extreme days for eight SAT phases. See text for the definition of SAT phases. The black dots denote the areas where SAT anomalies are statistically significant at the 95% confidence level.

T and Z anomalies regressed on PC1

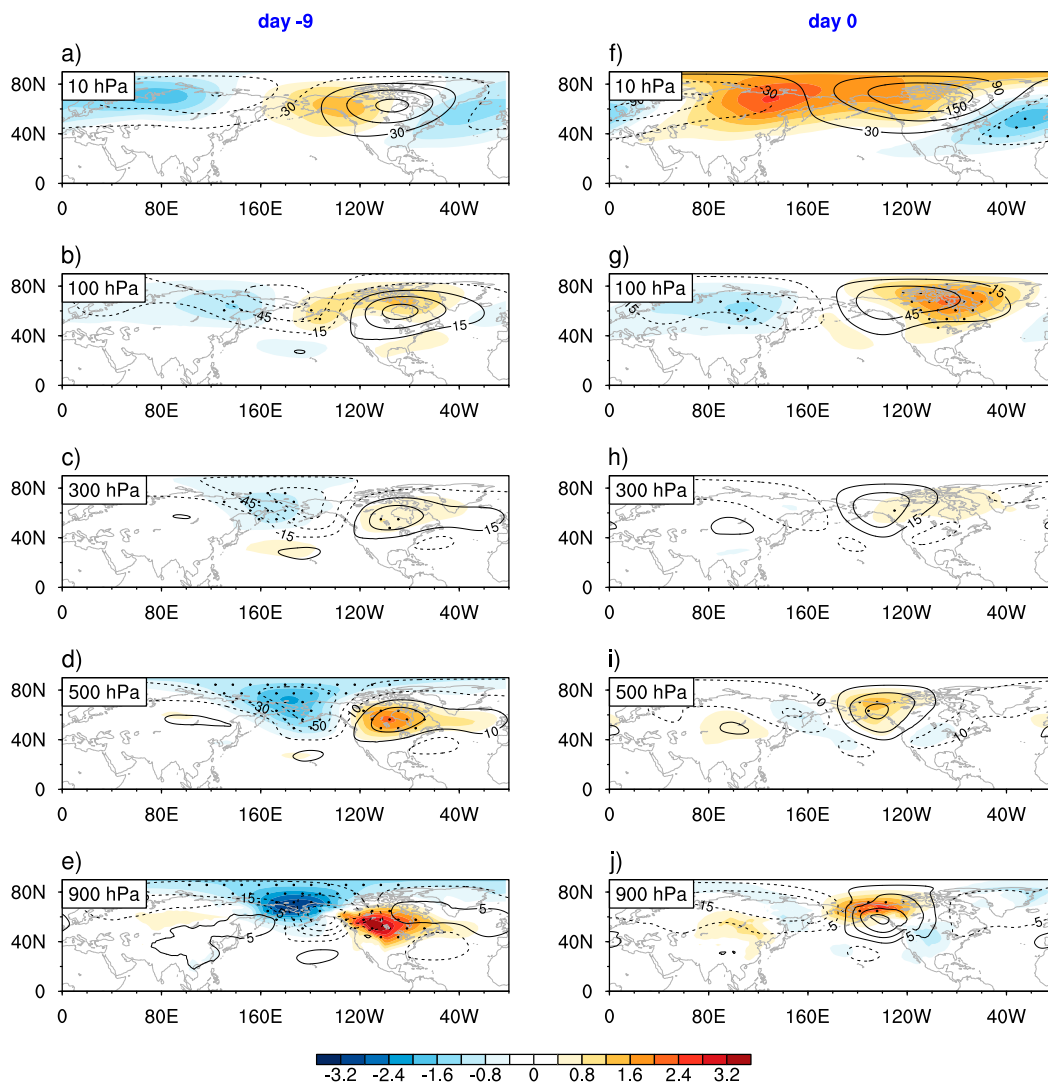


FIG. 10. Lag regressions of intraseasonal T ($^{\circ}\text{C}$; shading) and Z (gpm; contours) anomalies onto the normalized PC_1 at different vertical levels for (a)–(e) day -9 and (f)–(j) day 0 . The black dots denote the regressed T anomalies that are statistically significant at 95% confidence level.

leading SAT mode; U and V are winter mean zonal and meridional winds, respectively; f_0 is the Coriolis parameter; N^2 is the buoyancy frequency; p is the normalized pressure by 1000 hPa; and the subscripts represent partial derivatives in the corresponding x , y , and z directions.

Figure 14 displays vertical–longitude cross sections of 50° – 70°N averaged ψ' (shaded) and WAF associated with the leading intraseasonal SAT mode. At day -12 , while ψ anomalies are relatively weak, upward propagation of WAF from the lower to upper troposphere near 300 hPa is found near Alaska (Fig. 14a) that is mainly contributed by smaller-scale waves with zonal wavenumbers 2 and 3 (figure not shown). The upward WAF largely turns into eastward near 200 hPa toward the downstream

ridge area, leaving rather weak upward WAF into the stratosphere. After day -9 , upward propagation of planetary waves from the troposphere to the stratosphere is rapidly enhanced along with intensification of both negative and positive ψ anomalies in the stratosphere (Figs. 14b–d). This upward WAF into the stratosphere is dominated by the zonal-wave-number-1 component of ψ' and enhanced by the wavenumber-2 component (figure not shown), in accord with the upward propagation in the amplitude of the wavenumber-1 structure of Z anomalies in Fig. 11d. Enhanced upward propagation of planetary waves during this period is consistent with the westward tilt of trough and ridge lines with height, particularly in the upper troposphere and stratosphere (e.g., Kodera et al.

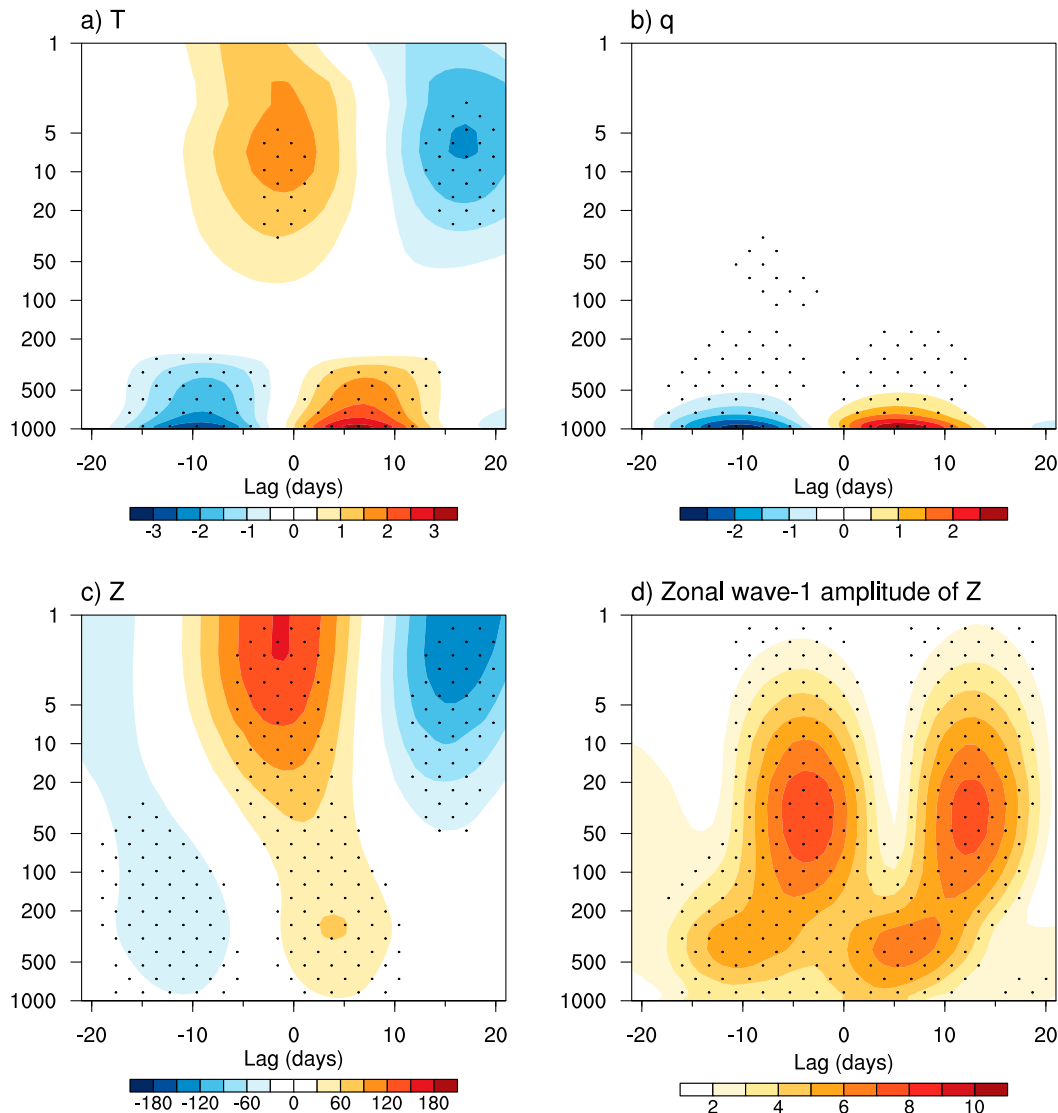


FIG. 11. Pressure–time cross sections of regressed (a) temperature (T , $^{\circ}\text{C}$) and (b) specific humidity (q , $10^{-4} \text{ kg kg}^{-1}$) anomalies averaged over 60° – 70°N , 160°E – 160°W , (c) geopotential height (Z , gpm) anomalies averaged over 50° – 70°N , 180° – 120°W , and (d) amplitude of zonal-wavenumber-1 component of Z anomalies (50° – 70°N averaged). The black dots denote the areas that are statistically significant at the 95% confidence level.

2008). While strong upward WAF is observed in the stratosphere at day -6 and day -3 , upward WAF in the lower troposphere is much weaker than that observed in day -12 and -9 , possibly due to weakened SAT and circulation anomalies during the transition phase of the intraseasonal SAT mode (Figs. 3c,d). Strong upward WAF into the stratosphere at day -6 and day -3 could be partially sustained by meridional WAF in the mid- to upper troposphere from the extratropical North Pacific into the Alaska region (e.g., at day -6 in Fig. 15a), via the Rossby wave teleconnection patterns induced by tropical convective activity over the western Pacific associated with the MJO (Fig. 7c).

After day 0, the upward propagation of planetary waves into the stratosphere is significantly suppressed to the east of the

date line; instead, the WAF is characterized by anomalous downward propagation in the upper troposphere (Figs. 14e,f). The suppressed vertical propagation is also in agreement with the less westward tilt of trough and ridge lines with altitude in the troposphere. Meanwhile, a descent of the ridge is observed between 180° and 120°W (Figs. 14e,f) associated with rapid development of a surface anomalous high over the Alaska region (Figs. 3e,f), signaling the initiation of the positive phase of the intraseasonal SAT mode. Amplification of local T and circulation anomalies associated with the intraseasonal SAT mode tends to reactivate the upward WAF in the lower troposphere near Alaska after day 3 (Figs. 14f,g). This upward WAF from the lower troposphere and horizontal WAF from both the ES and subtropical Pacific regions (Figs. 15b,c,e,f)

Z anomalies regressed on PC1 (500 hPa)

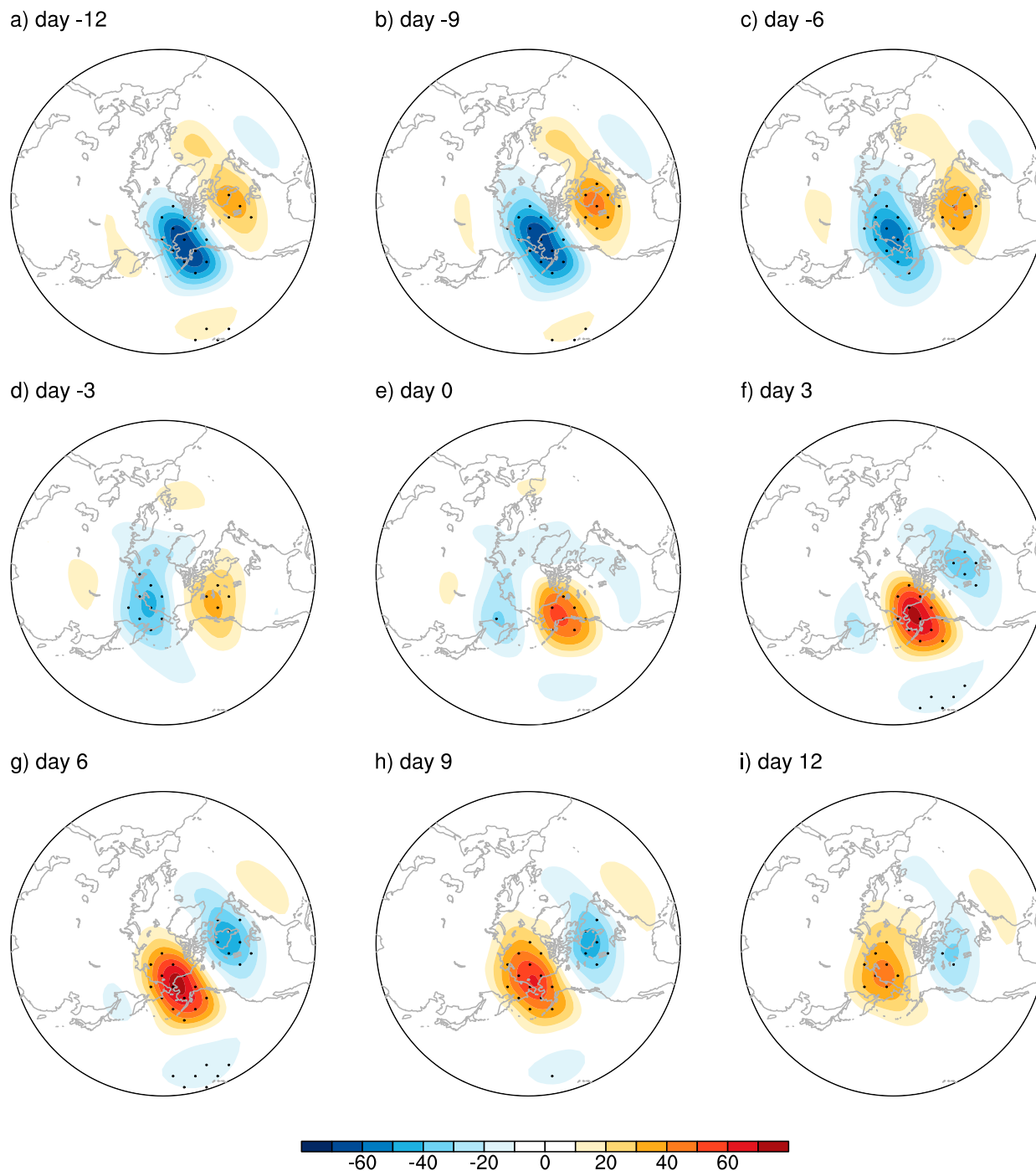


FIG. 12. Lag regressions of 500-hPa geopotential height (gpm) anomalies onto the normalized PC₁ from (a) day -12 to (i) day 12 with an interval of 3 days. The black dots denote the areas that are statistically significant at the 95% confidence level.

Z anomalies regressed on PC1 (5 hPa)

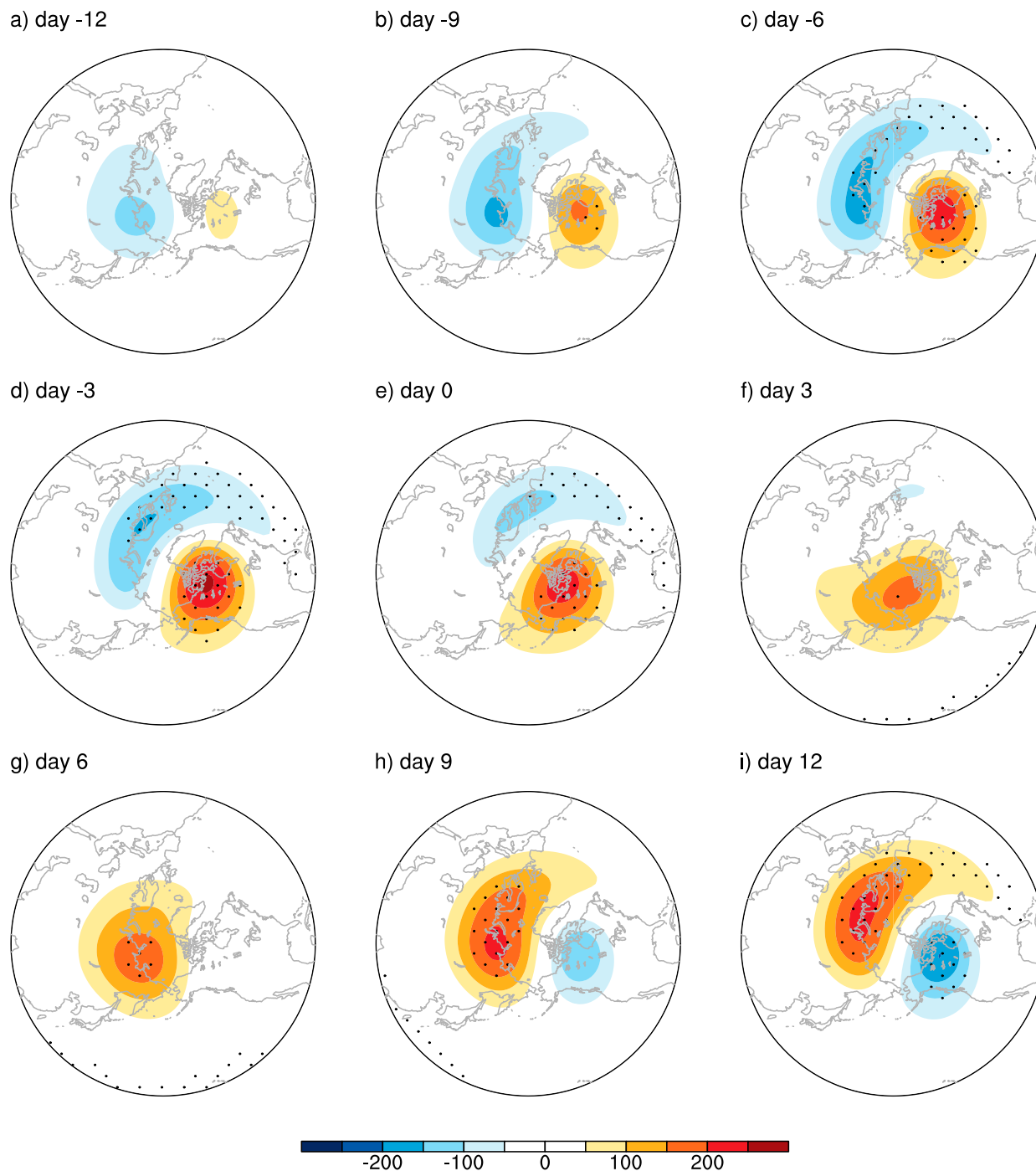


FIG. 13. As in Fig. 12, but for 5-hPa geopotential height anomalies.

converge in the upper troposphere over the ridge area near Alaska and then turn eastward and trigger a downstream trough over north Canada between 120° and 60°W (Fig. 14f). Development of the trough over north Canada further leads

to a slight westward shift of the ridge over Alaska after day 3 as clearly seen in Figs. 14f and 14g. After day 6, in association with the gradual enhancement of upward propagation of planetary waves (also see Fig. 11d), both the anomalous ridge and trough

Anomalous streamfunction and WAF associated with PC1 (50–70°N)

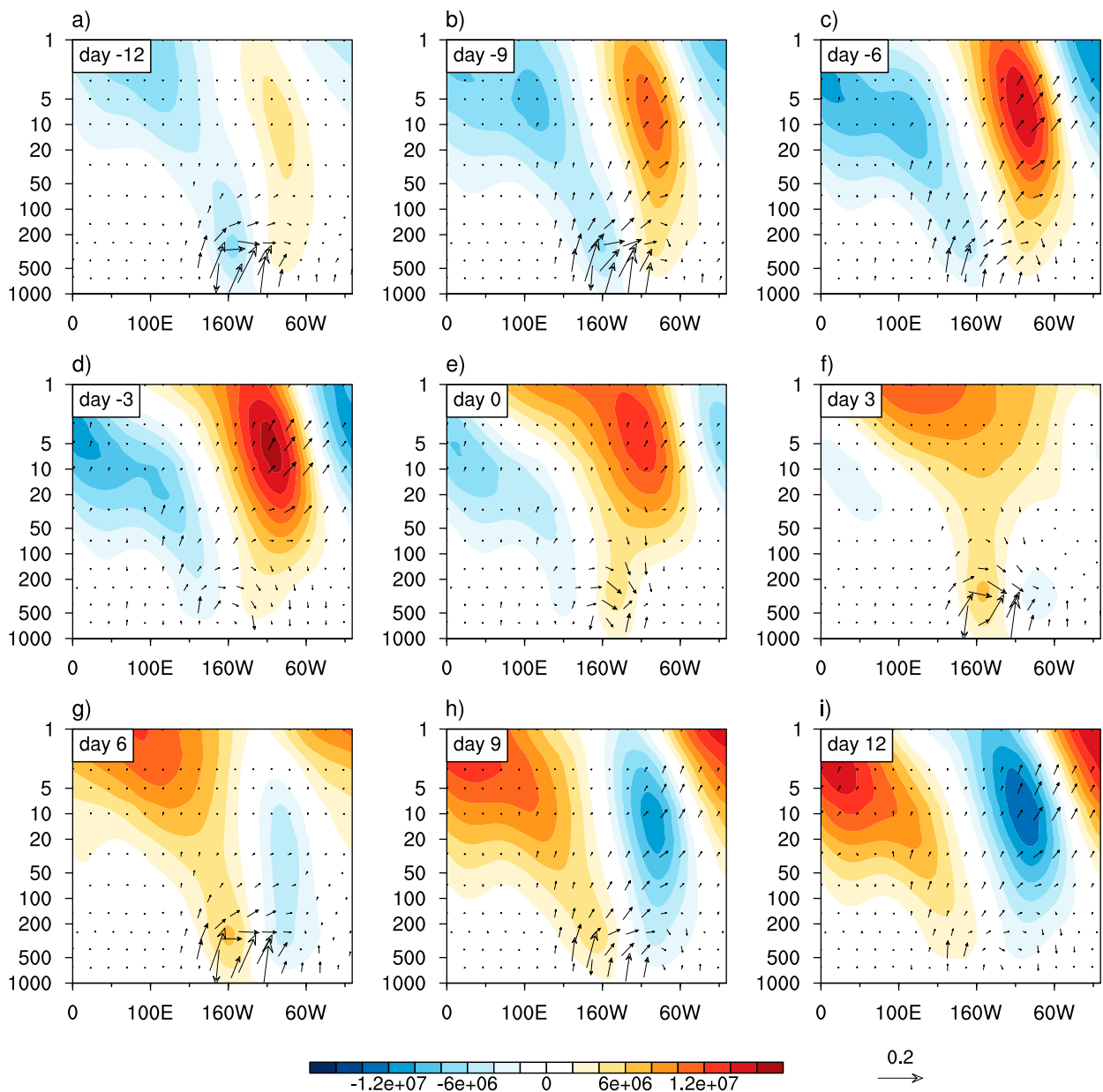


FIG. 14. Height–longitude evolution of regressed anomalies of streamfunction ($\text{m}^2 \text{s}^{-1}$; shading), vertical and zonal components of WAF (vectors; $\text{m}^2 \text{s}^{-2}$ for the horizontal component, and $2.5 \times 10^{-3} \text{m}^2 \text{s}^{-2}$ for the vertical component) averaged over $50^\circ\text{--}70^\circ\text{N}$ from (a) day –12 to (i) day 12 with an interval of 3 days. The magnitude of WAF at each level is scaled by the inverse of the square root of corresponding normalized pressure (Kodera et al. 2013). The 3D wave activity flux is calculated according to Takaya and Nakamura (2001).

are intensified in the upper troposphere and stratosphere (Figs. 14h–i), exhibiting similar evolution features as previously discussed for the negative phase of the intraseasonal SAT mode after day –12 but with an opposite sign in ψ . Note that the amplitude of the WAF associated with the intraseasonal SAT mode shown in Fig. 14 is about 20% of the typical intraseasonal WAF variability in the troposphere and

lower stratosphere, with the latter estimated by the standard deviation of daily WAF based on 10–90-day-filtered ψ (figure not shown).

These abovementioned interactive processes between the troposphere and stratosphere associated with establishment of anomalous surface high over the Alaska region after day –3 (Fig. 3d) largely resemble the formation processes of Pacific

Wave activity flux regressed on PC1

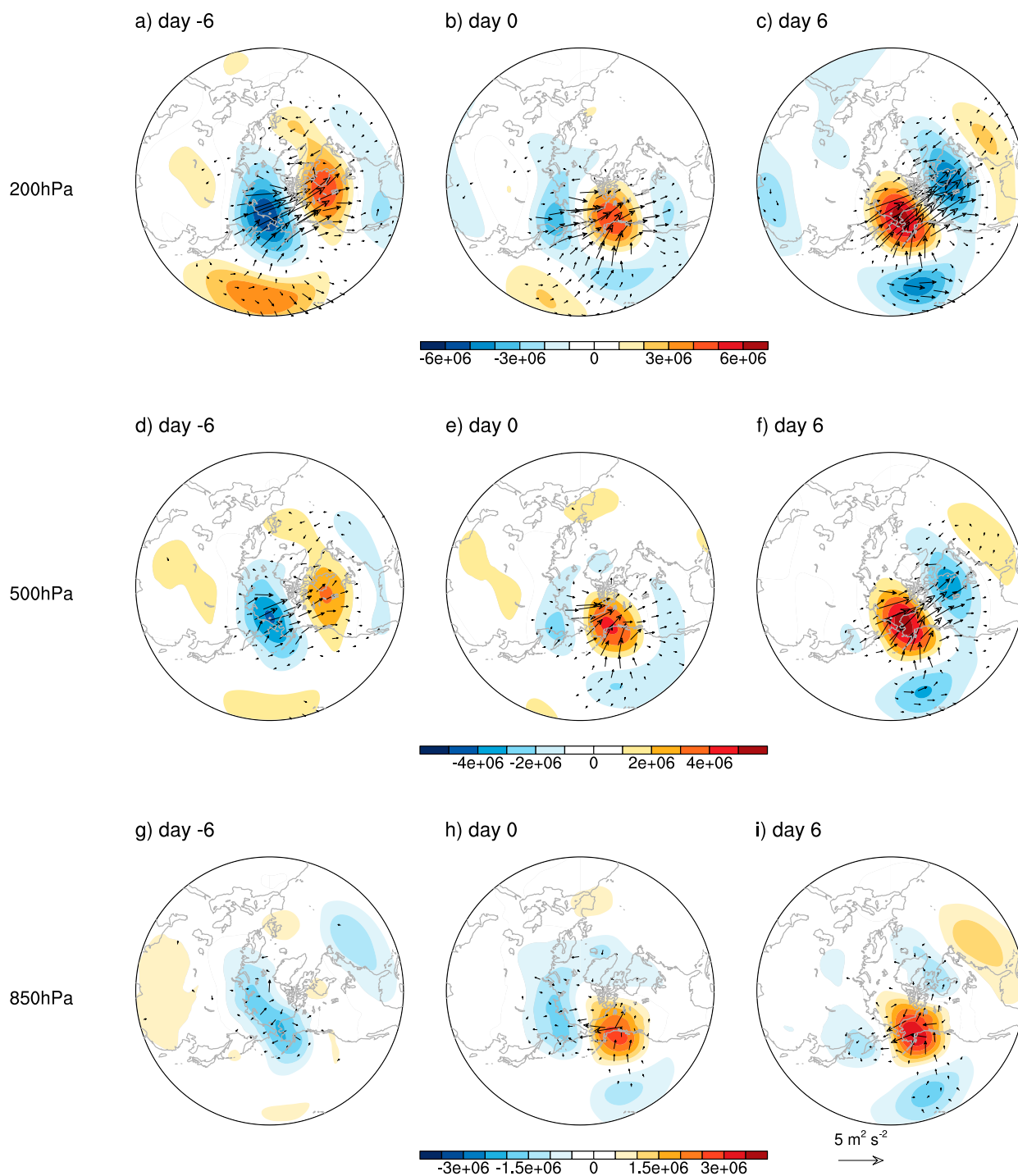


FIG. 15. The regressed anomalous streamfunction ($\text{m}^2 \text{s}^{-1}$; shading) and associated horizontal WAF ($\text{m}^2 \text{s}^{-2}$; vectors) at (left) day -6, (center) day 0, and (right) day 6 for the (a)–(c) 200-, (d)–(f) 500-, and (g)–(i) 850-hPa levels. Vectors are plotted only where WAF values are greater than $0.3 \text{ m}^2 \text{s}^{-2}$.

blockings (Kodera et al. 2008, 2016, 2013). Meanwhile, the anomalous surface high near Alaska during the positive phase of the intraseasonal SAT mode, for example, at day 3 (Fig. 3f), also bears a great similarity to the North Pacific blocking system previously reported (e.g., Renwick and Wallace 1996), suggesting a close linkage of the leading intraseasonal SAT variability over the NA sector discussed in this study to the blocking activity over the North Pacific.

Figure 15 further illustrates horizontal WAF and associated ω / at different phases of the intraseasonal SAT mode. As previously mentioned, both the local planetary wave activity near Alaska and meridional Rossby wave propagation from the subtropical North Pacific, particularly at 200 hPa, could play an important role in promoting the stratosphere–troposphere interaction over the mid- to high latitudes through vertical planetary wave propagation. The coherent vertical wave structure indicates a plausible vertical wave coupling between the troposphere and the stratosphere rather than the typical wave–zonal flow interaction during the downward influence of the stratospheric sudden warming events (e.g., Limpasuvan et al. 2004). However, it remains unknown whether the stratospheric processes are essential in sustaining the leading intraseasonal SAT mode, or they are just passive responses to tropospheric wave activity.

The influence of tropical convective activity associated with the MJO on the polar stratosphere as indicated by this study has also been proposed in several recent studies. For example, it was found that the poleward-propagating wave trains induced by MJO convection can propagate upward into the stratosphere and modulate stratospheric polar vortex intensity (e.g., Garfinkel et al. 2012, 2014; Schwartz and Garfinkel 2017; Kang and Tziperman 2018a,b). Enhanced convection over the western Pacific warm pool (day –10; Fig. 8) associated with the MJO tends to lead the stratospheric warming over the Alaska region by about one week (Fig. 11a), which is also in agreement with previous studies (e.g., Schwartz and Garfinkel 2017; Garfinkel and Schwartz 2017).

6. Summary and discussion

In this study, detailed characteristics of the dominant intraseasonal SAT variability mode over the NA sector during boreal winter are investigated. The leading intraseasonal SAT mode, identified by an EEOF analysis of 10–90-day-filtered SAT anomalies during 38 boreal winters (November–March) from 1979 to 2017, exhibits a dipole pattern with one center over central NA, and another over ES/Alaska with an opposite sign. This intraseasonal SAT mode bears great resemblance to the “warm-Arctic–cold-continent” pattern observed in the interannual variability of SAT over the NA sector. Therefore, improved understanding of this intraseasonal SAT mode will provide critical insights into physics regulating the observed interannual SAT variability over NA (e.g., Guan et al. 2020).

The leading intraseasonal SAT mode and associated anomalous circulation exert a significant influence on regional weather and climate extremes. During the positive phase of the intraseasonal SAT mode, defined by warming (cooling) anomalies over ES/Alaska (central NA), an anomalous surface high is observed over the Alaska region (Figs. 3f–h). Under this condition, sea ice concentration (SIC) is significantly reduced over CBS with

an amplitude of about 20% of local climatological value (Fig. 5). It is found that sea ice loss over CBS lags surface warming over ES/Alaska, which further slightly lags the southerly anomalous winds and related negative THF and DLWR over CBS (Fig. 6). Therefore, associated with this intraseasonal SAT mode, atmospheric circulation plays a critical role in driving both surface warming over ES/Alaska and sea ice loss over CBS.

Significantly reduced precipitation over the northwest coast of NA is observed during positive phases of the intraseasonal SAT mode (Figs. 7e–g), possibly due to horizontal moisture advection induced by the anomalous high near Alaska (Figs. 3e–g); meanwhile, enhanced precipitation over the North Pacific near the Hawaiian Islands is observed. Signals of the eastward-propagating MJO from the Indian Ocean to the western Pacific are detected associated with evolution of the intraseasonal SAT mode, with enhanced tropical convective activity over the western Pacific observed about one week prior to the stratospheric warming over ES/Alaska (Figs. 8, 11a). The stratospheric warming over ES/Alaska further leads surface warming over ES/Alaska associated with the positive phase of intraseasonal SAT mode by about 10 days (Fig. 11a). The tropical influence on the mid- to high latitudes is manifested by a clear Rossby wave teleconnection pattern extending from the western/central Pacific to NA at 200 hPa (Fig. 7). The intraseasonal SAT mode is found to be closely linked to extreme warm and cold events. Regions with positive (negative) SAT anomalies over the NA continent and the Arctic region near Alaska associated with the intraseasonal SAT mode agree well with frequent occurrence of warm (cold) extreme events (Fig. 9). All these results suggest that a reliable prediction of the intraseasonal SAT mode will be of great value for subseasonal prediction of extreme weather events over the NA sector.

It is further illustrated that the surface warming or cooling signals associated with the leading intraseasonal SAT mode are closely connected to T anomalies in a deep-tropospheric layer up to 300 hPa with a decreasing amplitude with height (Figs. 10, 11); meanwhile, enhanced (reduced) lower-tropospheric moisture is found to be coupled with tropospheric and surface warming (cooling), suggesting a positive role of moisture effect on intraseasonal temperature variability over mid- to high latitudes through a longwave radiative feedback as previously discussed.

Particularly noteworthy is the plausible role of the coupling between the troposphere and stratosphere for formation of the surface anomalous high or low over Alaska and Hudson Bay during the transition phase of the intraseasonal SAT mode. Analyses of 3D WAF indicate that the troposphere–stratosphere interactions involved with the intraseasonal SAT variability are via upward propagation of planetary waves to the stratosphere, as previously observed similarly during the formation of blockings (e.g., Kodera et al. 2013). During the negative phase of the intraseasonal SAT mode, enhanced upward propagation of planetary waves in the lower troposphere from the cyclonic circulation region near Alaska leads to amplification of ridge and trough in the upper troposphere and stratosphere. Subsequently, planetary waves are reflected back to the troposphere, inducing a ridge near Alaska and a trough near Hudson Bay over Canada and thus the transition from the negative to positive phase of the intraseasonal SAT mode. It is further illustrated that upward-propagating planetary waves near Alaska that influence stratospheric wave activities tend to have two different origins: one over the

ES/Alaska region associated with local intraseasonal variability, possibly resulting from instabilities by baroclinic energy conversion as previously reported (Sheng and Derome 1991; Cai et al. 2007), and another from the subtropical North Pacific associated with Rossby wave trains induced by tropical convective activity over the western Pacific warm pool region (Fig. 15).

This study suggests that interactions between troposphere and stratosphere over mid- to high latitudes through 3D propagation of planetary waves could possibly play an important role underlying the dominant intraseasonal SAT variability mode over NA, which has never been previously reported. However, it is difficult to determine whether the stratospheric processes are essential in sustaining the leading intraseasonal SAT mode based on observations alone. Moreover, the role of tropical MJO convective activity for the intraseasonal SAT variability as indicated by this study also needs to be verified. Further investigations on the essential physics regulating the leading intraseasonal SAT variability mode over the NA sector are warranted, for example, based on climate model experiments.

Acknowledgments. WG and XR are jointly supported by the National Key Research and Development Program of China (Grant 2018YFC1505903) and the National Natural Science Foundation of China (NSFC) (Grant 41621005), and XJ acknowledges support by the NOAA Climate Program Office under Awards NA15OAR4310098, NA15OAR4310177, and NA17OAR4310261. GC is supported by NSF Grant AGS-1832842. The ERA-Interim data can be taken from the website: <http://apps.ecmwf.int/datasets/>. The daily GPCP precipitation data can be assessed at <https://www.ncei.noaa.gov/data/global-precipitation-climatology-project-gpcp-daily/access/>. Sea ice concentration data from the National Snow and Ice Data Center Climate Data Record can be downloaded at <http://nsidc.org/data/g02202>.

REFERENCES

- Adler, R., J.-J. Wang, M. Sapiiano, G. Huffman, D. Bolvin, E. Nelkin, and NOAA CDR Program, 2017: Global Precipitation Climatology Project (GPCP) Climate Data Record (CDR), version 1.3 (daily). NOAA National Centers for Environmental Information, accessed 8 May 2020, <https://doi.org/10.7289/V5RX998Z>.
- Baxter, S., and S. Nigam, 2015: Key role of the North Pacific Oscillation–west Pacific pattern in generating the extreme 2013/14 North American winter. *J. Climate*, **28**, 8109–8117, <https://doi.org/10.1175/JCLI-D-14-00726.1>.
- , S. Weaver, J. Gottschalck, and Y. Xue, 2014: Pentad evolution of wintertime impacts of the Madden–Julian oscillation over the contiguous United States. *J. Climate*, **27**, 7356–7367, <https://doi.org/10.1175/JCLI-D-14-00105.1>.
- Blackport, R., J. A. Screen, K. van der Wiel, and R. Bintanja, 2019: Minimal influence of reduced Arctic Sea ice on coincident cold winters in mid-latitudes. *Nat. Climate Change*, **9**, 697–704, <https://doi.org/10.1038/s41558-019-0551-4>.
- Cai, M., S. Yang, H. M. Van Den Dool, and V. E. Kousky, 2007: Dynamical implications of the orientation of atmospheric eddies: A local energetics perspective. *Tellus*, **59A**, 127–140, <https://doi.org/10.1111/j.1600-0870.2006.00213.x>.
- Carrera, M. L., R. W. Higgins, and V. E. Kousky, 2004: Downstream weather impacts associated with atmospheric blocking over the northeast Pacific. *J. Climate*, **17**, 4823–4839, <https://doi.org/10.1175/JCLI-3237.1>.
- Casola, J. H., and J. M. Wallace, 2007: Identifying weather regimes in the wintertime 500-hPa geopotential height field for the Pacific–North American sector using a limited-contour clustering technique. *J. Appl. Meteor. Climatol.*, **46**, 1619–1630, <https://doi.org/10.1175/JAM2564.1>.
- Cassou, C., 2008: Intraseasonal interaction between the Madden–Julian oscillation and the North Atlantic Oscillation. *Nature*, **455**, 523–527, <https://doi.org/10.1038/nature07286>.
- Chamey, J. G., and P. G. Drazin, 1961: Propagation of planetary-scale disturbances from the lower into the upper atmosphere. *J. Geophys. Res.*, **66**, 83–109, <https://doi.org/10.1029/jz066i001p00083>.
- Clark, J. P., and S. Lee, 2019: The role of the tropically excited Arctic warming mechanism on the warm Arctic cold continent surface air temperature trend pattern. *Geophys. Res. Lett.*, **46**, 8490–8499, <https://doi.org/10.1029/2019GL082714>.
- Cohen, J., and Coauthors, 2014: Recent Arctic amplification and extreme mid-latitude weather. *Nat. Geosci.*, **7**, 627–637, <https://doi.org/10.1038/ngeo2234>.
- Collow, T. W., W. Wang, and A. Kumar, 2019: Reduction in northern midlatitude 2-m temperature variability due to Arctic sea ice loss. *J. Climate*, **32**, 5021–5035, <https://doi.org/10.1175/JCLI-D-18-0692.1>.
- Dai, Y., and B. Tan, 2019: Two types of the western Pacific pattern, their climate impacts, and the ENSO modulations. *J. Climate*, **32**, 823–841, <https://doi.org/10.1175/JCLI-D-17-0618.1>.
- Dee, D. P., and Coauthors, 2011: The ERA-Interim reanalysis: Configuration and performance of the data assimilation system. *Quart. J. Roy. Meteor. Soc.*, **137**, 553–597, <https://doi.org/10.1002/qj.828>.
- Ferranti, L., T. N. Palmer, F. Molteni, and E. Klinker, 1990: Tropical–extratropical interaction associated with the 30–60 day oscillation and its impact on medium and extended range prediction. *J. Atmos. Sci.*, **47**, 2177–2199, [https://doi.org/10.1175/1520-0469\(1990\)047<2177:TEIAWT>2.0.CO;2](https://doi.org/10.1175/1520-0469(1990)047<2177:TEIAWT>2.0.CO;2).
- Flournoy, M. D., S. B. Feldstein, S. Lee, and E. E. Clothiaux, 2016: Exploring the tropically excited Arctic warming mechanism with station data: Links between tropical convection and Arctic downward infrared radiation. *J. Atmos. Sci.*, **73**, 1143–1158, <https://doi.org/10.1175/JAS-D-14-0271.1>.
- Garfinkel, C. I., and C. Schwartz, 2017: MJO-related tropical convection anomalies lead to more accurate stratospheric vortex variability in subseasonal forecast models. *Geophys. Res. Lett.*, **44**, 10 054–10 062, <https://doi.org/10.1002/2017GL074470>.
- , S. B. Feldstein, D. W. Waugh, C. Yoo, and S. Lee, 2012: Observed connection between stratospheric sudden warmings and the Madden–Julian oscillation. *Geophys. Res. Lett.*, **39**, L18807, <https://doi.org/10.1029/2012GL053144>.
- , J. J. Benedict, and E. D. Maloney, 2014: Impact of the MJO on the boreal winter extratropical circulation. *Geophys. Res. Lett.*, **41**, 6055–6062, <https://doi.org/10.1002/2014GL061094>.
- Ghil, M., and K. Mo, 1991: Intraseasonal oscillations in the global atmosphere. Part I: Northern Hemisphere and tropics. *J. Atmos. Sci.*, **48**, 752–779, [https://doi.org/10.1175/1520-0469\(1991\)048<0752:IOITGA>2.0.CO;2](https://doi.org/10.1175/1520-0469(1991)048<0752:IOITGA>2.0.CO;2).
- Graversen, R. G., T. Mauritsen, M. Tjernstrom, E. Kallen, and G. Svensson, 2008: Vertical structure of recent Arctic warming. *Nature*, **451**, 53–56, <https://doi.org/10.1038/nature06502>.
- Guan, W., X. Jiang, X. Ren, G. Chen, and Q. Ding, 2020: Role of atmospheric variability in driving the “warm-Arctic, cold-continent” pattern over the North America sector and sea ice

- variability over the Chukchi-Bering Sea. *Geophys. Res. Lett.*, **47**, e2020GL088599, <https://doi.org/10.1029/2020gl088599>.
- Henderson, S. A., E. D. Maloney, and S.-W. Son, 2017: Madden-Julian oscillation Pacific teleconnections: The impact of the basic state and MJO representation in general circulation models. *J. Climate*, **30**, 4567–4587, <https://doi.org/10.1175/JCLI-D-16-0789.1>.
- Hoskins, B. J., and D. J. Karoly, 1981: The steady linear response of a spherical atmosphere to thermal and orographic forcing. *J. Atmos. Sci.*, **38**, 1179–1196, [https://doi.org/10.1175/1520-0469\(1981\)038<1179:TSLROA>2.0.CO;2](https://doi.org/10.1175/1520-0469(1981)038<1179:TSLROA>2.0.CO;2).
- Hu, W., P. Liu, Q. Zhang, and B. He, 2019: Dominant patterns of winter-time intraseasonal surface air temperature over the CONUS in response to MJO convections. *Climate Dyn.*, **53**, 3917–3936, <https://doi.org/10.1007/s00382-019-04760-x>.
- Jiang, X., and D. E. Waliser, 2009: Two dominant subseasonal variability modes of the eastern Pacific ITCZ. *Geophys. Res. Lett.*, **36**, L04704, <https://doi.org/10.1029/2008GL036820>.
- Jin, F., and B. J. Hoskins, 1995: The direct response to tropical heating in a baroclinic atmosphere. *J. Atmos. Sci.*, **52**, 307–319, [https://doi.org/10.1175/1520-0469\(1995\)052<0307:TDRTH>2.0.CO;2](https://doi.org/10.1175/1520-0469(1995)052<0307:TDRTH>2.0.CO;2).
- Johnson, N. C., and S. B. Feldstein, 2010: The continuum of North Pacific sea level pressure patterns: Intraseasonal, interannual, and interdecadal variability. *J. Climate*, **23**, 851–867, <https://doi.org/10.1175/2009JCLI3099.1>.
- Kang, W., and E. Tziperman, 2018a: The MJO-SSW teleconnection: Interaction between MJO-forced waves and the midlatitude jet. *Geophys. Res. Lett.*, **45**, 4400–4409, <https://doi.org/10.1029/2018GL077937>.
- , and —, 2018b: The role of zonal asymmetry in the enhancement and suppression of sudden stratospheric warming variability by the Madden-Julian oscillation. *J. Climate*, **31**, 2399–2415, <https://doi.org/10.1175/JCLI-D-17-0489.1>.
- Katz, R. W., and B. G. Brown, 1992: Extreme events in a changing climate: Variability is more important than averages. *Climatic Change*, **21**, 289–302, <https://doi.org/10.1007/BF00139728>.
- Kidston, J., A. A. Scaife, S. C. Hardiman, D. M. Mitchell, N. Butchart, M. P. Baldwin, and L. J. Gray, 2015: Stratospheric influence on tropospheric jet streams, storm tracks and surface weather. *Nat. Geosci.*, **8**, 433–440, <https://doi.org/10.1038/ngeo2424>.
- Kodera, K., H. Mukougawa, and S. Itoh, 2008: Tropospheric impact of reflected planetary waves from the stratosphere. *Geophys. Res. Lett.*, **35**, L16806, <https://doi.org/10.1029/2008GL034575>.
- , —, and A. Fujii, 2013: Influence of the vertical and zonal propagation of stratospheric planetary waves on tropospheric blockings. *J. Geophys. Res. Atmos.*, **118**, 8333–8345, <https://doi.org/10.1002/JGRD.50650>.
- , —, P. Maury, M. Ueda, and C. Claud, 2016: Absorbing and reflecting sudden stratospheric warming events and their relationship with tropospheric circulation. *J. Geophys. Res. Atmos.*, **121**, 80–94, <https://doi.org/10.1002/2015JD023359>.
- Kug, J.-S., J.-H. Jeong, Y.-S. Jang, B.-M. Kim, C. K. Folland, S.-K. Min, and S.-W. Son, 2015: Two distinct influences of Arctic warming on cold winters over North America and East Asia. *Nat. Geosci.*, **8**, 759–762, <https://doi.org/10.1038/ngeo2517>.
- Kushnir, Y., 1987: Retrograding wintertime low-frequency disturbances over the North Pacific Ocean. *J. Atmos. Sci.*, **44**, 2727–2742, [https://doi.org/10.1175/1520-0469\(1987\)044<2727:RWLFDO>2.0.CO;2](https://doi.org/10.1175/1520-0469(1987)044<2727:RWLFDO>2.0.CO;2).
- Lee, S., T. Gong, N. Johnson, S. B. Feldstein, and D. Pollard, 2011: On the possible link between tropical convection and the Northern Hemisphere Arctic surface air temperature change between 1958 and 2001. *J. Climate*, **24**, 4350–4367, <https://doi.org/10.1175/2011JCLI4003.1>.
- L'Heureux, M. L., and R. W. Higgins, 2008: Boreal winter links between the Madden-Julian oscillation and the Arctic Oscillation. *J. Climate*, **21**, 3040–3050, <https://doi.org/10.1175/2007JCLI1955.1>.
- Limpasuvan, V., D. W. J. Thompson, and D. L. Hartmann, 2004: The life cycle of the Northern Hemisphere sudden stratospheric warmings. *J. Climate*, **17**, 2584–2596, [https://doi.org/10.1175/1520-0442\(2004\)017<2584:TLCOTN>2.0.CO;2](https://doi.org/10.1175/1520-0442(2004)017<2584:TLCOTN>2.0.CO;2).
- Lin, H., 2015: Subseasonal variability of North American winter-time surface air temperature. *Climate Dyn.*, **45**, 1137–1155, <https://doi.org/10.1007/s00382-014-2363-6>.
- , 2018: Predicting the dominant patterns of subseasonal variability of wintertime surface air temperature in extratropical Northern Hemisphere. *Geophys. Res. Lett.*, **45**, 4381–4389, <https://doi.org/10.1029/2018GL077509>.
- , 2020: Subseasonal forecast skill over the northern polar region in boreal winter. *J. Climate*, **33**, 1935–1951, <https://doi.org/10.1175/JCLI-D-19-0408.1>.
- , and J. Derome, 1995: On the thermal interaction between the synoptic-scale eddies and the intraseasonal fluctuations in the atmosphere. *Atmos.–Ocean*, **33**, 81–107, <https://doi.org/10.1080/07055900.1995.9649525>.
- , and G. Brunet, 2009: The influence of the Madden-Julian oscillation on Canadian wintertime surface air temperature. *Mon. Wea. Rev.*, **137**, 2250–2262, <https://doi.org/10.1175/2009MWR2831.1>.
- , —, and J. Derome, 2009: An observed connection between the North Atlantic Oscillation and the Madden-Julian oscillation. *J. Climate*, **22**, 364–380, <https://doi.org/10.1175/2008JCLI2515.1>.
- Linkin, M. E., and S. Nigam, 2008: The North Pacific Oscillation–west Pacific teleconnection pattern: Mature-phase structure and winter impacts. *J. Climate*, **21**, 1979–1997, <https://doi.org/10.1175/2007JCLI2048.1>.
- Madden, R. A., and P. R. Julian, 1971: Detection of a 40–50 day oscillation in zonal wind in tropical Pacific. *J. Atmos. Sci.*, **28**, 702–708, [https://doi.org/10.1175/1520-0469\(1971\)028<0702:DOADOI>2.0.CO;2](https://doi.org/10.1175/1520-0469(1971)028<0702:DOADOI>2.0.CO;2).
- Martineau, P., G. Chen, and D. A. Burrows, 2017: Wave events: Climatology, trends, and relationship to Northern Hemisphere winter blocking and weather extremes. *J. Climate*, **30**, 5675–5697, <https://doi.org/10.1175/JCLI-D-16-0692.1>.
- Matsueda, S., and Y. Takaya, 2015: The global influence of the Madden-Julian oscillation on extreme temperature events. *J. Climate*, **28**, 4141–4151, <https://doi.org/10.1175/JCLI-D-14-00625.1>.
- Molteni, F., T. N. Stockdale, and F. Vitart, 2015: Understanding and modelling extra-tropical teleconnections with the Indo-Pacific region during the northern winter. *Climate Dyn.*, **45**, 3119–3140, <https://doi.org/10.1007/s00382-015-2528-y>.
- Mori, M., and M. Watanabe, 2008: The growth and triggering mechanisms of the PNA: A MJO-PNA coherence. *J. Meteor. Soc. Japan*, **86**, 213–236, <https://doi.org/10.2151/jmsj.86.213>.
- National Academies of Sciences, Engineering, and Medicine, 2016: *Next Generation Earth System Prediction: Strategies for Subseasonal to Seasonal Forecasts*. National Academies Press, 350 pp.
- North, G. R., T. L. Bell, R. F. Cahalan, and F. J. Moeng, 1982: Sampling errors in the estimation of empirical orthogonal functions. *Mon. Wea. Rev.*, **110**, 699–706, [https://doi.org/10.1175/1520-0493\(1982\)110<0699:SEITEO>2.0.CO;2](https://doi.org/10.1175/1520-0493(1982)110<0699:SEITEO>2.0.CO;2).
- Park, H.-S., S. Lee, S.-W. Son, S. B. Feldstein, and Y. Kosaka, 2015: The impact of poleward moisture and sensible heat flux on Arctic winter sea ice variability. *J. Climate*, **28**, 5030–5040, <https://doi.org/10.1175/JCLI-D-15-0074.1>.
- Peng, G., W. N. Meier, D. J. Scott, and M. H. Savoie, 2013: A long-term and reproducible passive microwave sea ice concentra-

- tion data record for climate studies and monitoring. *Earth Syst. Sci. Data*, **5**, 311–318, <https://doi.org/10.5194/essd-5-311-2013>.
- Plaut, G., and R. Vautard, 1994: Spells of low-frequency oscillations and weather regimes in the Northern Hemisphere. *J. Atmos. Sci.*, **51**, 210–236, [https://doi.org/10.1175/1520-0469\(1994\)051<0210:SOLFOA>2.0.CO;2](https://doi.org/10.1175/1520-0469(1994)051<0210:SOLFOA>2.0.CO;2).
- Renwick, J. A., and J. M. Wallace, 1996: Relationships between North Pacific wintertime blocking, El Niño, and the PNA pattern. *Mon. Wea. Rev.*, **124**, 2071–2076, [https://doi.org/10.1175/1520-0493\(1996\)124<2071:RBNPWB>2.0.CO;2](https://doi.org/10.1175/1520-0493(1996)124<2071:RBNPWB>2.0.CO;2).
- Riddle, E. E., M. B. Stoner, N. C. Johnson, M. L. L'Heureux, D. C. Collins, and S. B. Feldstein, 2013: The impact of the MJO on clusters of wintertime circulation anomalies over the North American region. *Climate Dyn.*, **40**, 1749–1766, <https://doi.org/10.1007/s00382-012-1493-y>.
- Schwartz, C., and C. I. Garfinkel, 2017: Relative roles of the MJO and stratospheric variability in North Atlantic and European winter climate. *J. Geophys. Res. Atmos.*, **122**, 4184–4201, <https://doi.org/10.1002/2016JD025829>.
- Screen, J. A., 2014: Arctic amplification decreases temperature variance in northern mid- to high-latitudes. *Nat. Climate Change*, **4**, 577–582, <https://doi.org/10.1038/nclimate2268>.
- , and I. Simmonds, 2010: The central role of diminishing sea ice in recent Arctic temperature amplification. *Nature*, **464**, 1334–1337, <https://doi.org/10.1038/nature09051>.
- Seo, K.-H., H.-J. Lee, and D. M. W. Frierson, 2016: Unraveling the teleconnection mechanisms that induce wintertime temperature anomalies over the Northern Hemisphere continents in response to the MJO. *J. Atmos. Sci.*, **73**, 3557–3571, <https://doi.org/10.1175/JAS-D-16-0036.1>.
- Sheng, J., and J. Derome, 1991: An observational study of the energy transfer between the seasonal mean flow and transient eddies. *Tellus*, **43A**, 128–144, <https://doi.org/10.3402/tellusa.v43i2.11921>.
- Sigmond, M., and J. C. Fyfe, 2016: Tropical Pacific impacts on cooling North American winters. *Nat. Climate Change*, **6**, 970–974, <https://doi.org/10.1038/nclimate3069>.
- Stan, C., and V. Krishnamurthy, 2019: Intra-seasonal and seasonal variability of the Northern Hemisphere extra-tropics. *Climate Dyn.*, **53**, 4821–4839, <https://doi.org/10.1007/s00382-019-04827-9>.
- , D. M. Straus, J. S. Frederiksen, H. Lin, E. D. Maloney, and C. Schumacher, 2017: Review of tropical–extratropical teleconnections on intraseasonal time scales. *Rev. Geophys.*, **55**, 902–937, <https://doi.org/10.1002/2016RG000538>.
- Straus, D. M., S. Corti, and F. Molteni, 2007: Circulation regimes: Chaotic variability versus SST-forced predictability. *J. Climate*, **20**, 2251–2272, <https://doi.org/10.1175/JCLI4070.1>.
- Sun, L., J. Perlwitz, and M. Hoerling, 2016: What caused the recent “warm Arctic, cold continents” trend pattern in winter temperatures? *Geophys. Res. Lett.*, **43**, 5345–5352, <https://doi.org/10.1002/2016GL069024>.
- Takaya, K., and H. Nakamura, 2001: A formulation of a phase-independent wave-activity flux for stationary and migratory quasi-geostrophic eddies on a zonally varying basic flow. *J. Atmos. Sci.*, **58**, 608–627, [https://doi.org/10.1175/1520-0469\(2001\)058<0608:AFOAPI>2.0.CO;2](https://doi.org/10.1175/1520-0469(2001)058<0608:AFOAPI>2.0.CO;2).
- Tanaka, S., K. Nishii, and H. Nakamura, 2016: Vertical structure and energetics of the western Pacific teleconnection pattern. *J. Climate*, **29**, 6597–6616, <https://doi.org/10.1175/JCLI-D-15-0549.1>.
- Trenberth, K. E., and D. J. Shea, 2005: Relationships between precipitation and surface temperature. *Geophys. Res. Lett.*, **32**, L14703, <https://doi.org/10.1029/2005GL022760>.
- Vecchi, G. A., and N. A. Bond, 2004: The Madden–Julian oscillation (MJO) and northern high latitude wintertime surface air temperatures. *Geophys. Res. Lett.*, **31**, L04104, <https://doi.org/10.1029/2003GL018645>.
- Vitart, F., 2014: Evolution of ECMWF sub-seasonal forecast skill scores. *Quart. J. Roy. Meteor. Soc.*, **140**, 1889–1899, <https://doi.org/10.1002/qj.2256>.
- , and F. Molteni, 2010: Simulation of the Madden–Julian oscillation and its teleconnections in the ECMWF forecast system. *Quart. J. Roy. Meteor. Soc.*, **136**, 842–855, <https://doi.org/10.1002/qj.623>.
- , and Coauthors, 2017: The Subseasonal to Seasonal (S2S) Prediction project database. *Bull. Amer. Meteor. Soc.*, **98**, 163–173, <https://doi.org/10.1175/BAMS-D-16-0017.1>.
- Wallace, J. M., and D. S. Gutzler, 1981: Teleconnections in the geopotential height field during the Northern Hemisphere winter. *Mon. Wea. Rev.*, **109**, 784–812, [https://doi.org/10.1175/1520-0493\(1981\)109<0784:TITGHF>2.0.CO;2](https://doi.org/10.1175/1520-0493(1981)109<0784:TITGHF>2.0.CO;2).
- Wang, J., H. Kim, D. Kim, S. A. Henderson, C. Stan, and E. D. Maloney, 2020: MJO teleconnections over the PNA region in climate models. Part I: Performance- and process-based skill metrics. *J. Climate*, **33**, 1051–1067, <https://doi.org/10.1175/JCLI-D-19-0253.1>.
- Weare, B. C., and J. S. Nasstrom, 1982: Examples of extended empirical orthogonal function analyses. *Mon. Wea. Rev.*, **110**, 481–485, [https://doi.org/10.1175/1520-0493\(1982\)110<0481:EOEOF>2.0.CO;2](https://doi.org/10.1175/1520-0493(1982)110<0481:EOEOF>2.0.CO;2).
- Wheeler, M. C., and H. H. Hendon, 2004: An all-season real-time multivariate MJO index: Development of an index for monitoring and prediction. *Mon. Wea. Rev.*, **132**, 1917–1932, [https://doi.org/10.1175/1520-0493\(2004\)132<1917:AARMMI>2.0.CO;2](https://doi.org/10.1175/1520-0493(2004)132<1917:AARMMI>2.0.CO;2).
- Xiang, B., S.-J. Lin, M. Zhao, N. C. Johnson, X. Yang, and X. Jiang, 2019: Subseasonal week 3–5 surface air temperature prediction during boreal wintertime in a GFDL model. *Geophys. Res. Lett.*, **46**, 416–425, <https://doi.org/10.1029/2018GL081314>.
- , Q. Sun, J.-H. Chen, N. C. Johnson, and X. Jiang, 2020: Subseasonal prediction of land cold extremes in boreal wintertime. *J. Geophys. Res. Atmos.*, **125**, e2020JD032670, <https://doi.org/10.1029/2020JD032670>.
- Yoo, C., S. Feldstein, and S. Lee, 2011: The impact of the Madden–Julian oscillation trend on the Arctic amplification of surface air temperature during the 1979–2008 boreal winter. *Geophys. Res. Lett.*, **38**, L24804, <https://doi.org/10.1029/2011GL049881>.
- , S. Lee, and S. B. Feldstein, 2012a: Mechanisms of Arctic surface air temperature change in response to the Madden–Julian oscillation. *J. Climate*, **25**, 5777–5790, <https://doi.org/10.1175/JCLI-D-11-00566.1>.
- , —, and —, 2012b: Arctic response to an MJO-like tropical heating in an idealized GCM. *J. Atmos. Sci.*, **69**, 2379–2393, <https://doi.org/10.1175/JAS-D-11-0261.1>.
- Zheng, C., E. K.-M. Chang, H.-M. Kim, M. Zhang, and W. Wang, 2018: Impacts of the Madden–Julian oscillation on storm-track activity, surface air temperature, and precipitation over North America. *J. Climate*, **31**, 6113–6134, <https://doi.org/10.1175/JCLI-D-17-0534.1>.
- Zhou, S., M. L'Heureux, S. Weaver, and A. Kumar, 2012: A composite study of the MJO influence on the surface air temperature and precipitation over the continental United States. *Climate Dyn.*, **38**, 1459–1471, <https://doi.org/10.1007/s00382-011-1001-9>.